AGU PUBLICATIONS

JGR

Journal of Geophysical Research: Oceans

RESEARCH ARTICLE

10.1002/2016JC012587

Special Section:
Dense Water Formations in the North Western Mediterranean: From the Physical Forcings to the Biogeochemical Consequences

Impact of the Mesoscale Dynamics on Ocean Deep Convection: The 2012–2013 Case Study in the Northwestern Mediterranean Sea

Robin Waldman[1], Marine Herrmann[2], Samuel Somot[1], Thomas Arsouze[3], Rachid Benshila[2], Anthony Bosse[4], Jerome Chanut[5], Herve Giordani[1], Florence Sevault[1], and Pierre Testor[6]

[1]Centre National de Recherches Meteorologiques, Meteo-France-CNRS, Toulouse, France, [2]Laboratoire d'Etudes Geophysiques et d'Oceanographie Spatiale, UMR5566, IRD-CNRS-CNES-Universite de Toulouse, Toulouse, France, [3]ENSTA ParisTech Universite Paris-Saclay and Laboratoire de Meteorologie Dynamique, Ecole Polytechnique, Palaiseau, France, [4]Geophysical Institute, University of Bergen, Bergen, Norway, [5]MERCATOR-Ocean, Toulouse, France, [6]Laboratoire d'Oceanographie et de Climat—Experimentations et Approches Numeriques, Centre National de Recherches Scientifiques (CNRS), Universite Pierre et Marie Curie, Paris, France

Abstract Winter 2012–2013 was a particularly intense and well-observed Dense Water Formation (DWF) event in the Northwestern Mediterranean Sea. In this study, we investigate the impact of the mesoscale dynamics on DWF. We perform two perturbed initial state simulation ensembles from summer 2012 to 2013, respectively, mesoscale-permitting and mesoscale-resolving, with the AGRIF refinement tool in the Mediterranean configuration NEMOMED12. The mean impact of the mesoscale on DWF occurs mainly through the high-resolution physics and not the high-resolution bathymetry. This impact is shown to be modest: the mesoscale does not modify the chronology of the deep convective winter nor the volume of dense waters formed. It however impacts the location of the mixed patch by reducing its extent to the west of the North Balearic Front and by increasing it along the Northern Current, in better agreement with observations. The maximum mixed patch volume is significantly reduced from 5.7 ± 0.2 to $4.2 \pm 0.6 \times 10^{13}$ m^3. Finally, the spring restratification volume is more realistic and enhanced from 1.4 ± 0.2 to $1.8 \pm 0.2 \times 10^{13}$ m^3 by the mesoscale. We also address the mesoscale impact on the ocean intrinsic variability by performing perturbed initial state ensemble simulations. The mesoscale enhances the intrinsic variability of the deep convection geography, with most of the mixed patch area impacted by intrinsic variability. The DWF volume has a low intrinsic variability but it is increased by 2–3 times with the mesoscale. We relate it to a dramatic increase of the Gulf of Lions eddy kinetic energy from 5.0 ± 0.6 to 17.3 ± 1.5 cm^2/s^2, in remarkable agreement with observations.

Key Points:
- Resolving mesoscale enhances deep convection along the Northern Current and reduces it along the North Balearic Front, improving its realism
- Mesoscale dynamics enhances the spring restratification rate, in better agreement with observations
- Mesoscale dynamics largely increases eddy kinetic energy and its realism, which activates the deep convection intrinsic variability

Correspondence to:
R. Waldman,
robin.waldman@meteo.fr

Citation:
Waldman, R., Herrmann, M., Somot, S., Arsouze, T., Benshila, R., Bosse, A., . . . Testor, P. (2017). Impact of the mesoscale dynamics on ocean deep convection: The 2012–2013 case study in the Northwestern Mediterranean Sea. *Journal of Geophysical Research: Oceans*, *122*. https://doi.org/10.1002/2016JC012587

Received 25 NOV 2016
Accepted 13 SEP 2017
Accepted article online 17 SEP 2017

1. Introduction

The Northwestern Mediterranean Sea (NWMed) is one of the rare Dense Water Formation (DWF) areas in the World ocean (Marshall & Schott, 1999). DWF and in particular the formation of Western Mediterranean Deep Water (WMDW), the main deep water mass in the Western Mediterranean Sea, constrains many biogeochemical and thermodynamical processes: nutrient renewal in upper layers and biological activity (Auger et al., 2014; D'Ortenzio et al., 2014; Herrmann et al., 2014; Tamburini et al., 2013), carbon and heat storage rate (Rugenstein et al., 2013; Santinelli et al., 2013; Winton et al., 2013) and therefore climate.

DWF has long been observed in the NWMed sea (Durrieu de Madron et al., 2013; Leaman & Schott, 1991; MEDOC-Group, 1970; Schott et al., 1996). It has a large interannual variability, with approximately half of the years with convection deeper than 1,000 m and a wide range of magnitudes (Herrmann et al., 2017; Mertens & Schott, 1998; Somot et al., 2016). From the numerous studies focusing on the driving mechanisms of DWF in the NWMed sea, a large consensus emerges on the dominant role of the atmospheric forcing in driving DWF (Béranger et al., 2010; Demirov & Pinardi, 2007; Herrmann & Somot, 2008; Herrmann et al., 2010; L'Hévéder et al., 2013, Sannino et al., 2009; Somot et al., 2016). Several studies also point out the impact of preconvection ocean preconditioning in modulating the DWF magnitude and properties (Grignon et al., 2010; Herrmann et al., 2010; Houpert et al., 2016; L'Hévéder et al., 2013; Somot et al., 2016).

In addition, several studies have characterized the impact of the mesoscale and submesoscale on DWF and the Mediterranean thermohaline circulation, including observational, theoretical, and modeling approaches. Regarding observations in the NWMed sea, most studies have focused on the generation and spreading of submesoscale coherent vortices (SCVs) throughout the DWF phenomenon. Testor and Gascard (2003) focus on the restratification phase and they find a mechanism of newly formed dense water export by anticyclonic SCVs with long lifetime. Testor and Gascard (2006) and Bosse et al. (2016) estimate that those SCVs contribute to $\sim 1/2$ of the dense water export outside of the NWMed basin. They suggest that such long-lived SCVs could introduce an ocean memory effect during the preconditioning phase of deep convection through their buoyancy signature. Finally, Bosse et al. (2015, 2016) confirm that SCVs are ubiquitous in the intermediate and deep layers of the NWMed sea. They quantify their Index of Stratification (IS, see section 2.3) signature of $\sim 0.1\ m^2/s^2$, which represents ~5–10% of the bottom IS in summer (Waldman et al., 2017).

Theoretical considerations have also permitted to predict the impact of mesoscale structures generated by baroclinic instabilities on DWF. Marshall and Schott (1999) argue that if the mixed patch (or deep convection area) is larger than the first Rossby radius of deformation, which is the case in the NWMed Sea, then it must break up into Rossby-radius-scale mesoscale eddies. Visbeck et al. (1996) find from scaling arguments that there is a competition between deep convection that dominates at short time scales (a few days) and baroclinic instability that dominates at longer time scales (weeks to months) and inhibits DWF. Laboratory experiments reveal that the development of baroclinic eddies can eventually stop DWF (Marshall & Schott, 1999).

Also, in the 1990s, idealized numerical simulations have aimed at characterizing the impact of the mesoscale on convection. Marshall and Schott (1999) find with idealized channel simulations that baroclinic instabilities develop after typically a few days of convection and inhibit it, which means that there is no strong scale separation between convective and baroclinic instability processes. Madec et al. (1991) used idealized NWMed Sea simulations and they found that the buoyancy advection by mesoscale eddies compensates the surface buoyancy loss and limits the maximum Mixed Layer Depth (MLD) during a DWF event. Such instabilities induce a transfer from available potential energy into kinetic energy, and the mesoscale kinetic energy becomes as high as the large-scale kinetic energy during the restratification phase. Finally, they found that the meandering is associated with vertical motion which leads to an overturning cell that restratifies the DWF region.

Finally, from the 2000s, a series of realistic numerical simulations of the NWMed Sea have been performed to quantify the impact of the mesoscale on DWF (Beuvier et al., 2012; Demirov & Pinardi, 2007; Herrmann et al., 2008). In all cases, they identify mesoscale eddies rather than SCVs that their resolution does not enable to represent. Demirov and Pinardi (2007) find at the eddy-permitting resolution that at depth, cyclonic eddies are formed following DWF through the baroclinic instability of the rim current separating old and new WMDW. They either remain in the NWMed Sea or are exported to the Algerian basin. On average, their flux is oriented southward and ultimately toward Gibraltar: as a consequence, they suggest that the Mediterranean thermohaline circulation is eddy-driven. Herrmann et al. (2008) find at eddy-resolving resolution that restratification is dominated by a southward export of new WMDW and that 1/3 of it is due to mesoscale eddies. They also compare an eddy-permitting and an eddy-resolving simulation, and they find that the latter reduces DWF, in better agreement with observations from Leaman and Schott (1991). However, their results are not exclusively attributable to horizontal resolution as both model configurations are fairly different. Finally, Beuvier et al. (2012) confirm at eddy-permitting resolution the role of eddies in the postconvection southward spreading of WMDW, although they suggest that at the 1/12° resolution this southward spreading is underestimated.

All the above mentioned studies addressing the role of the mesoscale on DWF in a realistic framework use eddy-permitting simulations or multiresolution simulations with fairly different models. Most of them focus on the postconvection restratification phase, whereas observations have suggested the potential impact of the mesoscale on the preconditioning and intense mixing phases of DWF. In addition, they document the mean impact of the mesoscale dynamics on DWF but the question of its role in activating the intrinsic variability (Grégorio et al., 2015; Penduff et al., 2011; Sérazin et al., 2015, 2016) of the DWF phenomenon remains open. Finally, the above mentioned studies focus on periods prior to the late 2000s to early 2010s when observations were scarce to evaluate the modeled DWF processes (Houpert et al., 2016). This study aims at complementing knowledge on the role of the mesoscale on deep convection by: developing a grid

refinement framework to address the impact of the mesoscale, all other parameters remaining identical, on deep convection; extending the analysis to all three phases of deep convection (preconditioning, intense mixing, and restratification); documenting with an ensemble simulation framework the impact of the mesoscale on the intrinsic variability of DWF; and simulating DWF during the exceptional measurement year 2012–2013 to evaluate the realism of models.

To summarize, in this study, we compare an eddy-permitting ensemble simulation to an eddy-resolving ensemble simulation using exactly the same ocean model core during the well-documented and convective 2012–2013 case study in order to diagnose and interpret the mean impact of the mesoscale on DWF and on its intrinsic variability during the main phases of deep convection. Section 2 describes the model, data, and methods used, section 3 diagnoses the impacts of the mesoscale on DWF and on its intrinsic variability, section 4 provides insight into the physical mechanisms involved, section 5 discusses results and their implications, and section 6 summarizes the main conclusions.

2. Model, Data, and Methods

2.1. Model

2.1.1. Eddy-Permitting Model

We use the ocean general circulation model NEMO (Madec, 2008) in a regional configuration of the Mediterranean Sea called NEMOMED12 (Figure 1). The configuration is identical to Waldman et al. (2017) who detail it comprehensively. NEMOMED12 horizontal resolution is $\delta x = 6.1 - 7.1$ km in the NWMed Sea, it has 75 vertical z-levels of resolution between 1 m at the surface and 130 m at the bottom and the time step is 720 s. In the NWMed Sea, the size of mesoscale eddies and meanders is typically between 30 and 80 km (Crépon et al., 1982; Millot, 1991), but it is variable over time and space and the first baroclinic Rossby radius was estimated to be as low as 1.2 km in the DWF area during winter 2012–2013 (Giordani et al., 2017). The model's far-dissipation range is $7\delta x = 42.5 - 50.0$ km (Marchesiello et al., 2011), it is therefore a mesoscale eddy-permitting ocean model in the NWMed Sea, mainly outside the deep convective region.

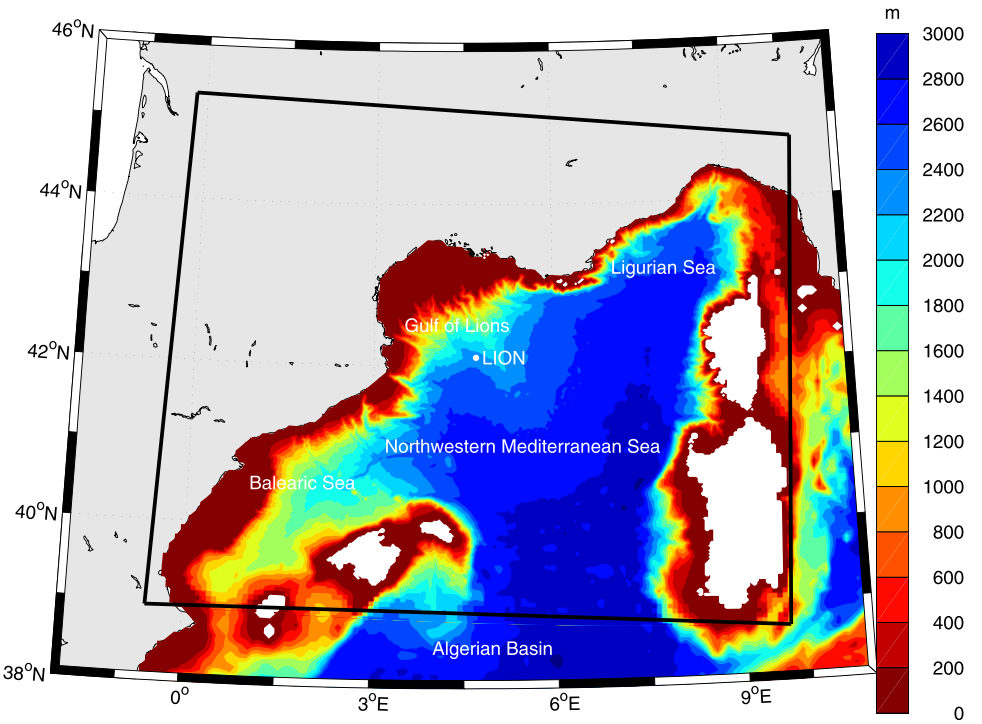

Figure 1. (top) Domain and associated bathymetry for NEMOMED12 and (bottom) its embedded NWMED36 configuration in the northwestern Mediterranean Sea. The locations of LION buoy and the main basins are displayed.

In terms of physics, we use in the horizontal a bilaplacian momentum diffusion operator ($-1.25\times10^{10}\mathrm{m}^4/\mathrm{s}$) to limit model diffusion at the mesoscale. For tracers, we use a Laplacian isoneutral dissusivity operator ($60\,\mathrm{m}^2/\mathrm{s}$) to parametrize mixing by unresolved eddies but no eddy-induced velocity parametrization (Gent & McWilliams, 1990) is added to permit the explicit resolution of baroclinic eddies. At the lateral boundaries, we use a free slip condition. In the vertical, mixing is driven by the Turbulent Kinetic Energy scheme (Gaspar et al., 1990) and by the parametrization of convection and bottom friction. For convection, we use the Enhanced Vertical Diffusion scheme which imposes a vertical mixing coefficient of $10\,\mathrm{m}^2/\mathrm{s}$ on tracers and momentum when static instabilities occur. Although very simple, this parametrization has proven successful to model deep convection in the NWMed Sea (Herrmann et al., 2008; Somot et al., 2016).

The model is forced at the surface by the dynamical downscaling of the ERA-Interim using the regional climate model ALADIN-Climate (Colin et al., 2010; Herrmann et al., 2011; Radu et al., 2008). This forcing has a 12 km resolution and is referred in the following as ALDERA (Hamon et al., 2016; Waldman et al., 2017). It provides momentum, water, and heat fluxes every 3 h over the 2012–2013 period. It is applied with a Newtonian sea surface temperature (SST) restoration of $-40\ \mathrm{W}/\mathrm{m}^2/\mathrm{K}$ to ensure thermal stability and to act as a first-order coupling term. West of the Gibraltar strait, we apply a Newtonian temperature, salinity, and sea level restoration toward ORAS4 reanalysis (Balmaseda et al., 2013). Finally, the river runoff climatology is taken from Ludwig et al. (2009) for the main river mouths listed in RivDis (Vörösmarty et al., 1996). The Black Sea runoff climatology is deduced from Stanev and Peneva (2001).

2.1.2. Eddy-Resolving Model

In addition, we use the two-way horizontal nesting tool AGRIF (Debreu et al., 2008; Djath et al., 2014a) in NEMOMED12 with a refinement factor of 3 in an extended NWMed Sea domain north of 38.8°N and west of 10°E (Figure 1). This model is named NWMED36 in the following. AGRIF is a two-way grid refinement tool which allows the NEMOMED12 model to impose lateral boundary conditions to the embedded NWMED36 model while at the same time updating the NEMOMED12 fields over the embedded domain by upscaling the NWMED36 fields. It has already been used in a number of regional oceanic studies focusing specifically on the dynamics of semienclosed seas (Djath et al., 2014b), on the impact of the mesoscale on the Labrador Sea DWF (Chanut et al., 2008), on the Atlantic Meridional Overturning Circulation (Biastoch et al., 2008; Talandier et al., 2014) and on eddy activity (Jouanno et al., 2012).

Table 1 summarizes both NEMOMED12 and NWMED36 configurations and Figure 1 displays both domains and bathymetries. NWMED36 resolution is $\delta x = 2.0-2.4$ km in the NWMed Sea, equivalent to an effective resolution of $7\delta x = 14.2-16.7$ km, it is therefore mesoscale eddy-resolving in the NWMed Sea. We also note that NWMED36 is eddy-permitting for SCVs whose diameter is typically 15 km (Bosse et al., 2015, 2016; Testor & Gascard, 2003, 2006). Its numerical configuration is identical to NEMOMED12 except for horizontal and isoneutral diffusion coefficients which are reduced to, respectively, $-0.25\times10^9\ \mathrm{m}^4/\mathrm{s}$ and $30\,\mathrm{m}^2/\mathrm{s}$ in order to explicitely resolve the mesoscale. Also, the time step is reduced to 240 s for numerical stability purposes. Finally, the bathymetry resolution is increased to be consistent to the physical variables resolution.

2.1.3. Simulations

Both configurations are initialized on 1 August 2012 using an ocean objective analysis introduced by Estournel et al. (2016). The first guess of the initial state is given by the MERCATOR-Ocean operational analysis. To improve the realism of the model initial conditions over the region of interest, 3-D corrections were added using MOOSE-GE summer 2012 cruise (Testor et al., 2012) and ARGO float (ARGO, 2000) data. Also, the initial mesoscale field is perturbed identically as in Waldman et al. (2017) to produce a 10 member ensemble at both resolutions in order to assess the impact of the mesoscale on the Intrinsic Ocean Variability (IOV) and the significance of its mean impact on DWF. We created 10 perturbed initial hydrologies by extracting the basin-scale potential temperature θ_{BS} and salinity S_{BS} from 1 August 2012 of Estournel et al. (2016) objective analysis and the mesoscale θ_{MS} and S_{MS} from 1 August of years between 1980 and 1989 of a twin hindcast NEMOMED12 similar to the free run in Hamon et al. (2016). For each model vertical level, θ_{BS} and S_{BS} are obtained by averaging each field over sliding windows of ±50 km in the zonal and meridional directions, and θ_{MS} and S_{MS} are the residual: $\theta_{MS}=\theta-\theta_{BS}$ and $S_{MS}=S-S_{BS}$. The largest mesoscale structures reach 80–100 km in the NWMed Sea (Millot, 1991), we therefore ensure that all the mesoscale signal is included in θ_{MS} and S_{MS}.

Waldman et al. (2017) evaluated this ensemble initial state which was found to be realistic at the large-scale and whose mesoscale perturbation modifies by up to 1/4 the basin-scale index of stratification (IS) from

Table 1
Summary Table of NEMOMED12 and NWMED36 Numerical Configurations

Domain	NEMOMED12 Mediterranean	NWMED36 Northwestern Mediterranean
Grid	ORCA12	ORCA36
Horizontal resolution (physics, bathymetry)	6.1–7.1 km	2.0–2.4 km
Vertical resolution	1 m (surface) to 130 m (bottom)	
Temporal resolution	720 s	240 s
Lateral advection	Momentum: invariant vectorial form and energy/enstrophy-conserving Tracers: total variance dissipation scheme	
Lateral diffusion	Momentum: bilaplacian horizontal, $Kh_m = -1.25 \times 10^{10} m^4/s$ Tracers: Laplacian isoneutral, $Kh_t = 60\ m^2/s$	$Kh_m = -0.25 \times 10^9 m^4/s$ $Kh_t = 30\ m^2/s$
Lateral boundary	Free slip	
Free surface	Filtered fast waves, linear elliptic solver	
Turbulence	Turbulent Kinetic Energy scheme, variable Prandtl number	
Convection	Enhanced Vertical Diffusion for tracers and momentum, $Kz_{EVD} = 10\ m^2/s$	
Bottom friction	Quadratic, function of currents and of tidal TKE	
Background mixing	$Kz_m = 10^{-4} m^2/s$ and $Kz_t = 10^{-5} m^2/s$	
Atlantic boundary	Newtonian restoring for θ, S, and SSH toward ORAS4 (Balmaseda et al., 2013)	
Rivers	Surface freshwater flux from RivDis and Ludwig et al. (2009)	
Dardanelles	Surface freshwater flux from Stanev and Peneva (2001)	
Atmospheric forcing	Flux ALDERA 12 km, 3 h: nonsolar, solar, water and momentum Newtonian restoring toward ERA-INTERIM SST ($-40\ W/m^2/K$)	
Initial conditions	Large-scale ($L > 100$ km) from Estournel et al. (2016) objective analysis Mesoscale perturbation ($L < 100$ km) from a twin NEMOMED12 hindcast	

Estournel et al. (2016). They also evaluated NEMOMED12 ensemble simulation on the 2012–2013 period and showed its realism in terms of chronology, geography and magnitude, and hydrology of the DWF event. The atmospheric forcing ALDERA was also shown to be realistic in representing the chronology, spatial patterns, and surface atmospheric properties of the strong wind events Mistral and Tramontane which dominate winter air-sea interactions. In particular, Herrmann and Somot (2008) and Herrmann et al. (2011) have highlighted the necessity of applying a high-resolution atmospheric forcing to represent those strong wind events. The main biases that were evidenced are: an overestimation of latent heat loss at surface by ALDERA forcing; a southward shift of the DWF area with respect to observations; a cold anomaly in the signature of deep waters associated to DWF; and an underestimation of the restratification rate. Therefore, in this study we only use observations to evaluate the realism of the mesoscale impact on DWF in NWMED36 model.

2.2. Data

Observations used in this study are summarized in Table 2 and their location and time of acquisition is shown in Figure 2. We aim at estimating from them the chronology, hydrological properties, geography, magnitude of the 2012–2013 deep convective winter as well as the associated eddy activity.

To document the chronology and hydrological properties of deep convection, we analyze LION buoy and mooring data. LION meteorological buoy (Caniaux et al., 2017) is located within the DWF area (42.102°N 4.703°E, Figure 1). It provides all the near-surface observable meteorological parameters and radiative fluxes (incoming longwave and shortwave radiation) since 2012. The data were validated following the procedure described by Caniaux et al. (2017), and hourly turbulent fluxes (latent and sensible heat fluxes, and wind stress) were computed with the COARE3.0 flux algorithm (Fairall et al., 2003) for the period 1 August 2012 to 30 June 2013. Due to missing sequences of values and rejected data, the record of fluxes is limited to only 1808 hourly fluxes (21% of the 2012–2013 period). It also measures the sea surface temperature (SST) and salinity (SSS). Subsurface temperature measurements anchored at LION buoy are finally combined with LION deep mooring temperature measurements (Testor et al., 2016) to estimate the MLD daily time series from the temperature criterion of Houpert et al. (2016).

Table 2
Synthetic Table of Observations Used in this Study: the Instruments, Physical Measurements Used Here, Diagnostics Deduced From Them and Analyzed Here and Sampling Periods

Instrument	Measurement	Diagnostic	Period
LION buoy and mooring	Sea surface temperature (SST), salinity (SSS), near-surface wind ($V_{3.5m}$), atmospheric temperature ($T_{3.5m}$) and specific humidity ($q_{3.5m}$), downward radiative fluxes (longwave Q_{LWd} and shortwave Q_{SWd}), temperature profile (θ)	10 m wind (V_{10m}), net heat flux (Q_{tot}), sea surface density ($SS\rho$), mixed layer depth (MLD)	Continuous
Ship cruise CTDs	(θ,S) profiles	MLD maps, mixed patch volume (V_{MLD}), dense water volume ($V_{29.11}$), dense water formation (V_{dens}) and restratification ($V_{Restrat}$) volumes	Four cruises centered in time on 1 August 2012, 12 February 2013, 13 April 2013, and 24 June 2013
Glider profiles	(θ,S) profiles and 0–1,000 m average velocities ($U_{0-1000m}$ and $V_{0-1000m}$)	MLD maps, V_{MLD}, eddy kinetic energy (EKE)	Throughout the 2012–2013 period
ARGO profiles	(θ,S) profiles	MLD maps, V_{MLD}	Throughout the 2012–2013 period

To document eddy activity, we use glider-based Eddy Kinetic Energy (EKE) measurements which were shown to be more accurate than altimetry in this small Rossby radius region (Escudier et al., 2013). In the 2012–2013 period, up to six gliders were simultaneously deployed, mostly along four radials covering the NWMed Sea basin (Estournel et al., 2016). We estimate the EKE using the depth-average currents deduced from each glider dive. Only dives deeper than 800 m (gliders dive to a maximal depth of 1,000 m), located in the open-ocean (at least 30 km away from the 500 m isobath) and in the Gulf of Lions area ($6°E > lon > 4°E$ and $lat > 41.25°N$) were considered and represent 1,552 relevant current estimations (over a total number of 5,183 dives) between 1 September 2012 and 30 June 2013. The average velocity over a sliding window of width $L = 100$ km along the glider track was removed in order to deduce the mesoscale velocity and compute the EKE (see section 2.3).

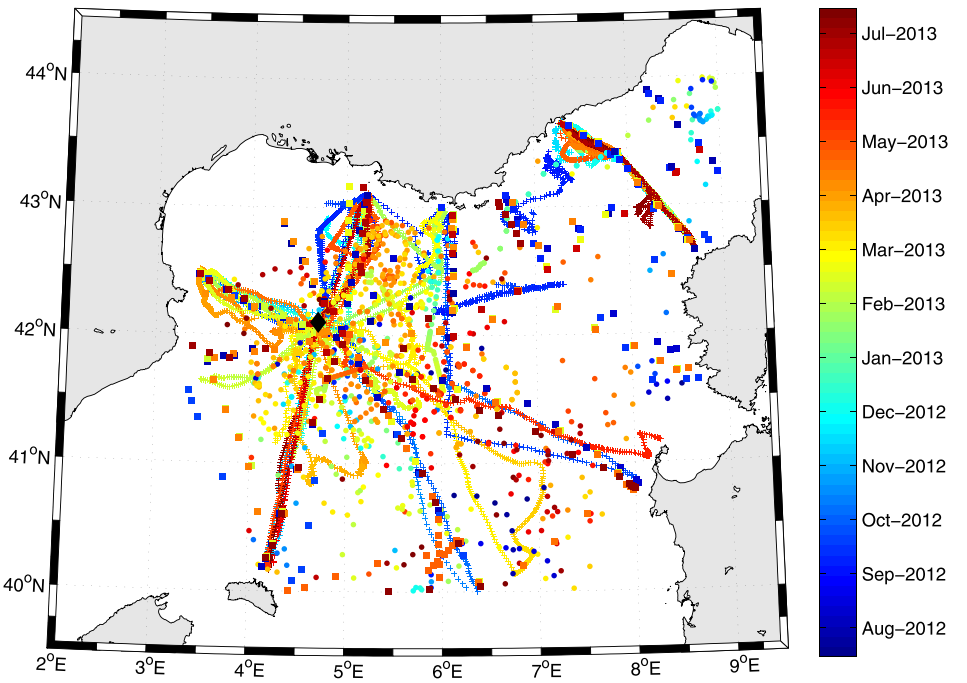

Figure 2. Map of all observations used in this study: LION buoy and mooring (diamond), ship cruise CTD casts (squares), glider profiles (crosses), and ARGO profiles (circles). Colors symbolize the time of data acquisition except for LION buoy which provides a continuous sampling in time.

Finally, to document the geography and magnitude of deep convection, we use two complementary approaches based either on the dense water volume or on the mixed layer depth (MLD) estimation (see section 2.3). The dense water volume was estimated as in Waldman et al. (2016) using four basin-scale CTD ship measurements centered in time on 1 August 2012, 12 February 2013, 13 April 2013, and 24 June 2013 including $68-82$ CTD casts (Conan, 2013; Testor, 2013; Testor et al., 2012, 2013). The seasonal evolution of the open-sea ($H > 2,000$ m) dense water volume was inferred to deduce a DWF volume and a spring restratification volume. As a complementary approach, we use the MLD estimations to deduce the mixed patch area and volume during winter 2013. For that we combine all hydrological profiles available from the LION mooring, ship cruise (428 profiles), and glider (11,188 profiles) measurements plus the available ARGO profiles (1,063 profiles) to construct a time-varying MLD objective analysis. The observed mixed layer depth is objectively interpolated using a bathymetry-following correlation function (Bohme & Send, 2005). At first the objective analysis is performed with large spatial (100 km) and temporal (30 days) decorrelation scales in order to reconstruct the basin-scale and seasonal evolution of the mixed patch. Then a second step is performed using smaller decorrelation scales (15 km and 10 days) in order to capture the mesoscale and high-frequency variability of the mixed patch. The mixed layer is analyzed every 10 days during the intense mixing phase (January to March 2013). We deduce from these measurements the mixed patch extent when the largest convection is measured (10–19 February 2013) and its annual maximum extent (temporal composite). Note that glider profiles only reach 1,000 m depth, therefore when the measured MLD exceeds 1,000 m it is extrapolated using LION mooring data. None of the analysis methods uses a first guess from a model to ensure the independence of results with respect to numerical simulations.

2.3. Methods

2.3.1. DWF and Restratification Volumes

This study aims at quantifying the DWF volume in the NWMed Sea in models and observations. For that we compute both the mixed patch volume and dense water volume. Both estimates have been commonly used in the Mediterranean Sea (see Waldman et al., 2016, for a review). As argued by Waldman et al. (2017), both diagnostics physically differ: the mixed patch volume directly results from vertical mixing and it is intermittent during the deep convection events, whereas the dense water volume also results from the postconvection lateral advection and interior mixing and it increases continuously throughout the deep convection events. The mixed patch is defined as the area where MLD $> 1,000$ m, which is the average observed upper limit of the WMDW layer on 1 August 2012 (Waldman et al., 2017). The MLD is estimated following Waldman et al. (2017) as the depth where the Index of Stratification IS$=0.01$ m^2/s^2, with:

$$\mathrm{IS}(-z) = -\frac{g}{\rho_0}\int_{-z}^{0} z\frac{\partial \sigma_0}{\partial z}dz$$

quantifying the surface buoyancy flux necessary to mix the water column from surface to depth $-z$. g is the gravity acceleration, ρ_0 is the reference density, and σ_0 is the potential density with reference depth at the surface. A convective volume V_{MLD} (m^3) is deduced:

$$V_{\mathrm{MLD}} = \int\int_{\mathrm{MLD}>1000} \mathrm{MLD}(x,y)dxdy$$

The dense water volume is defined as:

$$V_{29.11} = \iiint_{\sigma_0 > 29.11 \mathrm{kg/m^3}} dxdydz$$

Waldman et al. (2016) showed from observations that during the 2012–2013 DWF event, the DWF volume is maximal for $\sigma_0 = 29.11$ kg/m^3, which is therefore the relevant isopycnal to quantify the dense water formation rate. In numerical simulations, the convective volume V_{dens} is deduced from the difference between the maximum $V_{29.11}$ during the intense mixing phase and its minimum during the preconditioning phase:

$$V_{dens} = max_{Int.Mix.}(V_{29.11}) - min_{Precond}(V_{29.11})$$

In observations, Waldman et al. (2016) showed that only the difference between the summer 2012 and spring 2013 period allows to estimate the DWF volume:

$$V_{dens} = V_{29.11}(12\ \text{April}\ \ 2013) - V_{29.11}(1\ \ \text{August}\ \ 2012)$$

although they quantified the maximum DWF volume to be 69% larger than this summer to spring value. The volume difference between spring and summer 2013 is an estimate of the restratification (or spreading) volume:

$$V_{Restrat} = V_{29.11}(24\ \text{June}\ \ 2013) - V_{29.11}(12\ \text{April}\ \ 2013)$$

2.3.2. Diapycnal Water Mass Transformations

In order to identify the mechanisms driving water mass transformations during DWF, we compute a water mass transformation diagnostic as a function of σ_0. It has first been introduced by Walin (1977) for diahaline transformations, it has then been adapted by Walin (1982) for diathermal transformations and by Tziperman (1986) for diapycnal transformations. It was then implemented in the Mediterranean Sea by (Bozec et al., 2008; Herrmann et al., 2008; Somot et al., 2006; Tziperman & Speer, 1994; Waldman et al., 2017). The dense water volume for a given density σ_0 is defined as:

$$V(\sigma_0) = \iiint_{\sigma(x,y,z)>\sigma_0} dxdydz$$

The computation of its variation between two dates d_1 and d_2 gives an estimate of the diapycnal transformation volume (DT, m^3) as:

$$\text{DT} = max_{\sigma_0}(|V(\sigma_0, d_2) - V(\sigma_0, d_1)|)$$

It quantifies the largest volume transformation occurring in the σ_0 space, which is particularly relevant during deep convection because it gives an estimate of the DWF rate (Herrmann et al., 2008; Somot et al., 2006; Waldman et al., 2017).

We follow Herrmann et al. (2008) and Waldman et al. (2017) in decomposing the daily dense water volume trend in the NWMed Sea (north of 40°N and west of 9°E) into four terms: a net volume variation V, a surface formation Su, a lateral transport T, and an interior mixing M, all in m^3 so that:

$$V = Su + T + M$$

Su quantifies the surface volume flux resulting from densification by surface buoyancy fluxes: it is deduced from the surface buoyancy flux and the surface density field. T is computed from the lateral volume advection across the NWMed Sea boundaries: Spain—Menorca, Menorca—Sardinia, and Corsica—Ligurian coast. Finally, M is the residual from the formula $M = V - Su - T$. It includes all mixing processes occurring within the NWMed basin, both explicit and numerical. Also, we follow Waldman et al. (2017) by decomposing the 2012–2013 period into three DWF phases: preconditioning, intense mixing, and restratification. Intense mixing starts on 5 January 2013 when Su becomes nonnegligible at $\sigma_0 = 29.11\ kg/m^3$ in NEMOMED12 (first day with $Su > 10^{11}\ m^3/d$ at $\sigma_0 = 29.11\ kg/m^3$ level), and it ends on 24 March 2013 when Su becomes negligible (last day with $Su > 10^{11}\ m^3/d$ at $\sigma_0 = 29.11\ kg/m^3$ level). As a consequence, we define preconditioning between 1 August 2012 and 4 January 2013 and restratification between 25 March 2013 and 30 June 2013.

2.3.3. Eddy Kinetic Energy

The EKE is computed from the vertical-mean horizontal velocity above 1,000 m depth $\mathbf{U_{0-1000m}}$. This allows for model evaluation with glider measurements. The specific kinetic energy KE (m^2/s^2), is defined as:

$$\text{KE} = 1/2\,\mathbf{U_{0-1000m}}^2$$

Following Herrmann et al. (2008), we decompose the KE into a large-scale KE and a mesoscale KE which corresponds to, respectively, the mean KE (MKE) and the EKE. Velocities are averaged over sliding windows of width $L = 100$ km in zonal and meridional directions, so that:

$$\langle \mathbf{U_{0-1000m}} \rangle (x,y,t) = \frac{1}{L^2} \int_{x-L/2}^{x+L/2} \int_{y-L/2}^{y+L/2} \mathbf{U_{0-1000m}}(x',y',t) dy' dx'$$

and

$$\mathbf{U_{0-1000m}}^*(x,y,t) = \mathbf{U_{0-1000m}}(x,y,t) - \langle \mathbf{U_{0-1000m}} \rangle (x,y,t)$$

are, respectively, the basin-scale and mesoscale velocities above 1,000 m depth. The MKE and EKE are deduced from:

$$MKE = 1/2 \langle \mathbf{U_{0-1000m}} \rangle^2$$

and

$$EKE = 1/2 \, \mathbf{U_{0-1000m}}^{*2}$$

This ensures that all mesoscale (up to ~80–100 km, Millot, 1991) and smaller-scale dynamical structures are included in the EKE.

In addition, we compute a standing (also named stationary) and transient EKE (respectively, SEKE and TEKE) in order to assess the respective contributions of the mean and transient mesoscale structures to the NWMed Sea KE. This decomposition has previously been used to characterize the Antarctic Circumpolar Current dynamics (Dufour et al., 2012; Thompson & Naveira Garabato, 2014). The mesoscale velocity $\mathbf{U_{0-1000m}}^*(x,y)$ is averaged over sliding time windows of $T = 6$ months, so that:

$$\overline{\mathbf{U_{0-1000m}}^*}(x,y,t) = \frac{1}{T}\int_{t-T/2}^{t+T/2} \mathbf{U_{0-1000m}}^*(x,y,t')dt'$$

and

$$(\mathbf{U_{0-1000m}}^*)'(x,y,t) = \mathbf{U_{0-1000m}}^*(x,y,t) - \overline{\mathbf{U_{0-1000m}}^*}(x,y,t)$$

are, respectively, the standing and transient mesoscale velocities above 1,000 m depth. Finally, the SEKE and TEKE are deduced from:

$$SEKE = 1/2 \, \overline{\mathbf{U_{0-1000m}}^*}^2$$

and

$$TEKE = 1/2 \, (\mathbf{U_{0-1000m}}^*)'^2$$

3. How Does the Mesoscale Impact Dense Water Formation?

3.1. Mean Mesoscale Impact on DWF

Figure 3 displays the evolution of the near-surface wind $|V|_{10m}$, the net heat flux Q_{tot}, surface hydrology (sea surface temperature SST, salinity SSS, and density SSρ) and the MLD observed at LION location and in the NEMOMED12 and NWMED36 ensembles, between 1 December 2012 and 30 April 2013. The MLD is computed for model evaluation purposes with Houpert et al. (2016) method. It is defined from the surface to 300 m as the depth where temperature differs by more than 0.1°C with respect to the 10 m temperature, and from 300 m to the bottom as the depth where it differs by more than 0.01°C with respect to the 300 m temperature. Atmospheric conditions are dominated by strong surface winds and cooling throughout the period, accurately simulated by ALDERA forcing despite an overestimation of intense heat fluxes. As a consequence, ocean deep convection occurs intermittently from 26 January 2013 to 18 March 2013 with a mixed layer reaching the ocean bed. During those events, surface hydrology stabilizes to the WMDW properties of ~13.0°C, 38.48 psu, and 29.11 kg/m^3.

The DWF events are well simulated on average by both NEMOMED12 and NWMED36. In the following, we refer to significant differences between both simulation ensembles when their significativity level has $p > 0.99$, using a bilateral Students t test. During the intense mixing events, the surface hydrology is very similar at both resolutions. The mesoscale slightly inhibits the late January DWF event, but the main difference occurs during the restratification phase. From 15 March 2013 to 30 April 2013, the SSS and SSρ experience a smaller decrease when the mesoscale is resolved, in better agreement with observations. The low salinity signature in NEMOMED12 might be related to a southward bias of the Northern Current (NC) which advects low salinity waters near the surface at LION buoy (see section 4).

Figure 4 displays the mixed patch area in observations and in both simulation ensembles, in the 10–19 February 2013 period and as an annual maximum. In observations, the DWF area is located off the Gulf of Lions, at 3.5–6.5°E and 41–42.5°N. The corresponding surface, denoted A_{MLD} by Waldman et al. (2017), reaches, respectively, 23,100 km^2 and 32,500 km^2 in both periods. All quantitative diagnostics related to DWF are

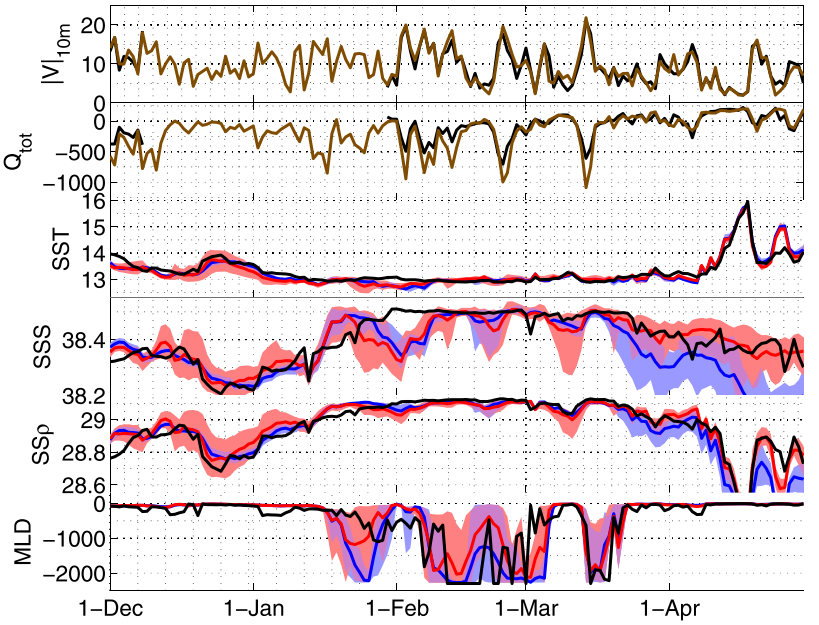

Figure 3. In the plot, black lines represent LION buoy/mooring data, brown ALDERA forcing, blue and red show, respectively, NEMOMED12 and NWMED36 simulation ensembles (ensemble mean, minimum, and maximum). From top to bottom: daily time series of near-surface wind $|V|_{10m}$ and net surface heat flux Q_{tot}, sea surface temperature (SST), salinity (SSS) and density (SSρ) and mixed layer depth (MLD) at LION location between 1 December 2012 and 30 April 2013.

given in Table 3. The modeled DWF area in the 10 February 2013 to 19 February 2013 period (Figure 4a) shows a large impact of the mesoscale. Whereas the mixed patch extends south to 41°N in NEMOMED12, it only extends to 41.5°N in NWMED36, in better agreement with observations. The mean MLD is reduced with the mesoscale (significant area in gray) in an even larger area at 4–5°E and 41–42°N. The impact of the mesoscale on the annual maximum mixed patch (Figure 4b) is however low on average. We still identify a significant DWF decrease to the south at 4–5°E and 40.5–41.2°N. It is located further south than Figure 4a, probably as a consequence of the mixed patch southward extension after 19 February 2013 at both resolutions. This area is located to the west of the North Balearic Front (NBF), it is therefore referred to as NBF-W in the following. We identify three other areas where the mesoscale significantly impact DWF: an increase at 5–5.6°E and 42.2–42.6°N, an increase at 6.4–6.9°E and 41.6–42.1°N and a decrease at 7.8–8.2°E and 43–43.3°N. Those areas are located, respectively, along the NC, to the east of the NBF and in the Ligurian Sea, we therefore refer to them as NC, NBF-E, and L areas. The DWF increase in the NC area and its decrease in the NBF-W and L areas are in good agreement with observations.

Figure 5 displays the estimates of V_{MLD} and $V_{29.11}$ in observations and their daily time series in both simulation ensembles. In observations, $V_{MLD}=4.1\times10^{13}m^3$, which is larger by 70% than Waldman et al. (2017) V_{MLD} estimate. Such a discrepancy is mostly due to the lack of glider observations in Waldman et al. (2017) quantification, therefore we believe that this study provides a more robust estimate. The $V_{29.11}$ evolution gives a larger value of $V_{dens}=4.5\pm1.1\times10^{13}$ m^3, and Waldman et al. (2016) deduced from it an annual maximum DWF volume of $V_{dens}=7.6\pm1.6\times10^{13}m^3$. Finally, the $V_{29.11}$ decrease between 13 April 2013 and 24 June 2013 gives an estimate of $V_{Restrat}=-2.6\pm1.1\times10^{13}$ m^3 (Figure 5b). Such DWF and restratification volumes define an intense to exceptional deep convection year (see Waldman et al., 2016, for a review of previous estimates of DWF rates).

In models, the V_{MLD} follows approximately the chronology of the MLD at LION buoy (Figure 3) during the intense mixing phase of deep convection. It is however decreased by the mesoscale from late January to late February. At the dates of observations, it reaches $2.4\pm0.3\times10^{13}$ m^3 in NWMED36, lower by 44% than in NEMOMED12, increasing the model bias. The annual maximum V_{MLD} is reduced by 26% with the mesoscale, reaching $4.2\pm0.6\times10^{13}$ m^3, confirming that the mesoscale reduces the time-integral DWF rate. The $V_{29.11}$ increases throughout the intense mixing phase at both resolutions. It is significantly lower in NWMED36 from late January to 10 February 2013, however in the 11 February 2013 to 20 March 2013

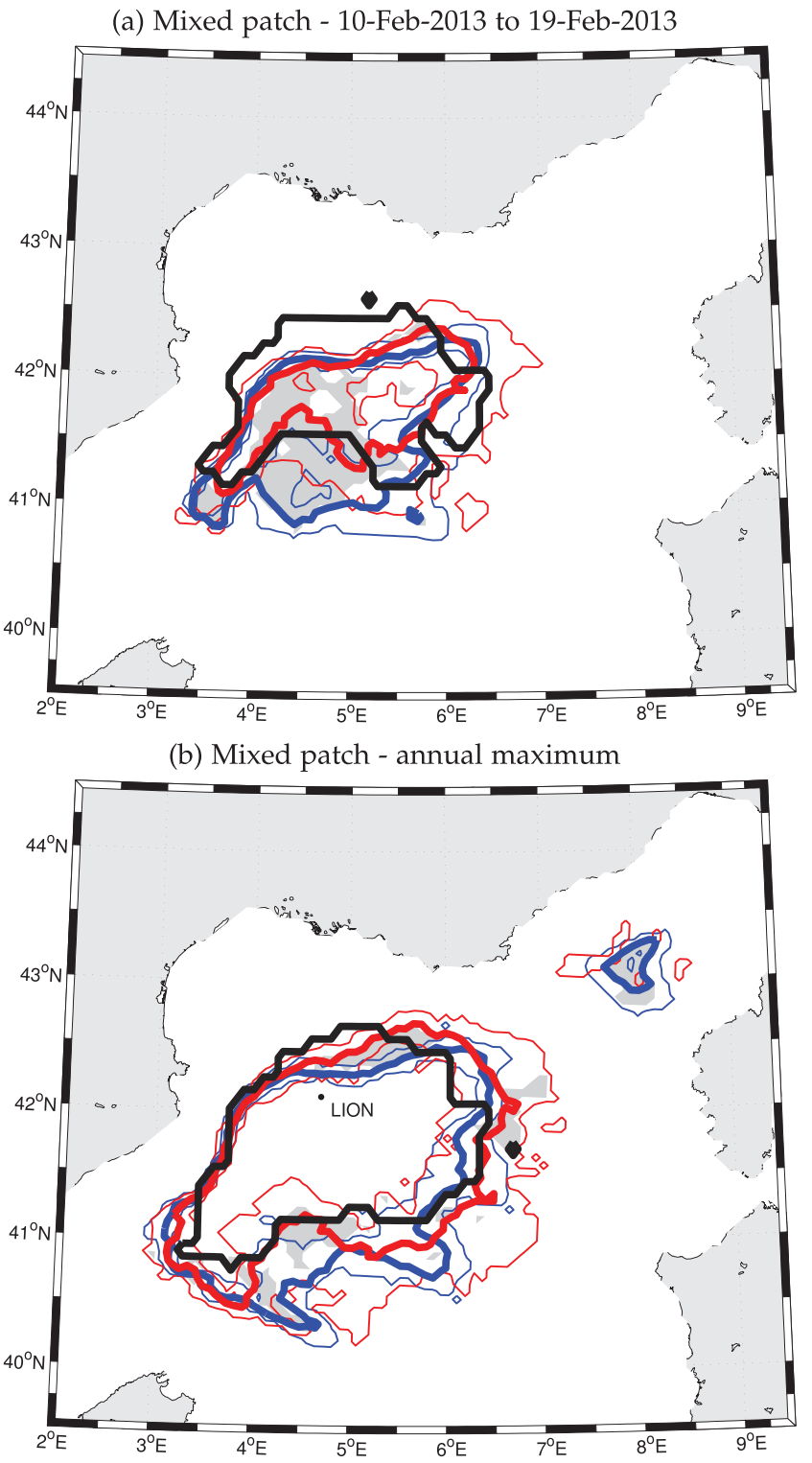

Figure 4. (a) Mixed patch area (MLD > 1,000 m) from observations (black), NEMOMED12 (blue), and NWMED36 (red) ensembles, 10–19 February 2013 average. In both simulations, the ensemble mean (bold), minimum (thin), and maximum (thin) areas are displayed. The 99% significance level (Student's *t* test, two sided) for ensemble mean differences is displayed in gray. (b) Same as Figure 4a but the mixed patch is computed as a composite from the annual maximum MLD.

Table 3
Large-Scale Estimates Related to the 2012–2013 Dense Water Formation (DWF) Event in Observations, NEMOMED12 and NWMED36 Ensembles

	Observations	NEMOMED12	NWMED36	Impact of mesoscale
V_{MLD} ($10^{13}m^3$)	4.1	4.2 ± 0.1	2.4 ± 0.3	Mixed patch reduction
V_{MLD} max (10^{13} m^3)		5.7 ± 0.2	4.2 ± 0.6	Mixed patch reduction
DF (%)		47	65	Intrinsic variability increase
Circ (km)		$1,114 \pm 71$	$1,277 \pm 75$	Stronger mixed patch meanders
V_{dens} ($10^{13}m^3$)	4.5 ± 1.1	3.3 ± 0.2	3.1 ± 0.4	
V_{dens} max ($10^{13}m^3$)	7.6 ± 1.6	5.4 ± 0.2	5.7 ± 0.4	
$V_{Restrat}$ ($10^{13}m^3$)	-2.6 ± 1.1	-1.4 ± 0.2	-1.8 ± 0.2	Restratification increase
$DT_{precond}$ ($10^{13}m^3$)		-2.4 ± 0.0 ($29.102\,kg/m^3$)	-2.6 ± 0.1 ($29.102\,kg/m^3$)	
DT_{mix} ($10^{13}m^3$)		5.8 ± 0.2 ($29.114\,kg/m^3$)	5.5 ± 0.4 ($29.112\,kg/m^3$)	
$DT_{restrat}$ ($10^{13}m^3$)		-1.9 ± 0.2 ($29.120\,kg/m^3$)	-2.3 ± 0.2 ($29.110\,kg/m^3$)	Restratification increase
EKE (cm^2/s^2)	17.7 ± 3.6	5.0 ± 0.6	17.3 ± 1.5	Eddy activity increase

Note. The DWF volume is estimated as the mixed patch volume V_{MLD} (with MLD > 1,000 m) and the dense water volume V_{dens} (at $29.11\,kg/m^3$) at the dates of observations (respectively, 10–19 February 2013 and between 1 August 2012 and 13 April 2013) and their annual maximum. The dispersive fraction DF is the fraction of the deep convection area where at least two members of the ensemble disagree on the occurrence of convection, and the mixed patch circumference *Circ* is the length of the MLD = 1,000 m contour around the mixed patch. The spring restratification volume is computed between observation dates 13 April 2013 and 24 June 2013. The diapycnal transformation volumes (DT) are computed at the density of maximum volume transformation (also indicated), with the preconditioning phase before 5 January 2013, the restratification phase after 24 March 2013 and the intense mixing phase in between. The average EKE is computed in the Gulf of Lions (4°E< lon < 6°E and lat > 41.25°N) on average between 1 September 2012 and 30 June 2013. The ± symbol represents the 95% confidence interval (V_{dens}, V_{dens} max, and *Restrat*.) or the standard deviation (EKE) in observations and the ensemble standard deviation in models.

period it is not significantly different at both resolutions. As a consequence, the evaluation of the modeled V_{dens} from 1 August 2012 to 13 April 2013 shows no significant impact of the mesoscale. We also note that in NWMED36, V_{dens} is larger by 63% than V_{MLD}, which provides a physical rationale for the discrepancy between both estimates in observations. Therefore, results from V_{MLD} and $V_{29.11}$ agree on a DWF reduction by the mesoscale from late January to 10 February 2013 and on insignificant differences in the 1–18 March 2013 period, but they disagree on the significance of the DWF reduction between 11 February 2013 and 28 February 2013. They also disagree on the annual maximum DWF volume, as V_{dens} shows no significant impact of the mesoscale ($5.7 \pm 0.4 \times 10^{13}$ m^3 as compared to $5.4 \pm 0.2 \times 10^{13}$ m^3). Finally, the modeled restratification volume is significantly increased by 29% when the mesoscale dynamics is resolved, reaching $-1.8 \pm 0.2 \times 10^{13}$ m^3, in better agreement with observations. To summarize, the representation of the mesoscale has opposite effects between the intense mixing phase and the restratification phase: it reduces the magnitude of the former and intensifies the latter.

3.2. Mesoscale Impact on the Intrinsic Variability of Deep Convection

At LION buoy (Figure 3), high-frequency variability is visible in observed surface hydrology, which can be related to the eddy activity from the unstable northern current located to the north. The intrinsic variability of sea surface properties is increased with the mesoscale, with an average ensemble standard deviation (STD) increase over the simulation period of, respectively, +56%, +20%, and +30% for the SST, SSS, and SSρ. However, the IOV of MLD is stable at both resolutions, with only a 5% increase with the mesoscale, which confirms results from Waldman et al. (2017) regarding the impact of IOV on DWF at LION buoy.

Over the whole NWMed Sea, we quantify the impact of the mesoscale on the intrinsic variability of the annual maximum mixed patch area (Figure 4b and Table 3) by computing the mixed patch dispersive fraction (DF, Waldman et al., 2017) and its circumference (Circ, Table 3). The DF measures the fraction between the dispersive mixed patch area (at least one ensemble member does not simulate DWF) and the total mixed patch area (at least one member simulates DWF): $DF = \frac{\max(A_{MLD}) - \min(A_{MLD})}{\max(A_{MLD})}$. Note that these surfaces are obtained from spatial composites of all members, so that: $\min(A_{MLD})$ is the area where all members simulate DWF, and $\max(A_{MLD})$ is the area where at least one member simulates DWF. The Circ is a proxy for the magnitude of rim current meanders around the mixed patch. Both the DF and Circ increase with the mesoscale: the DF reaches 65% (38% increase) and the Circ reaches 1277 ± 75 km (15% increase). This means that the mesoscale increases the modulation of the DWF geography by the IOV, and as a consequence, most of the 2013 event DWF area is impacted by IOV. Also, the mesoscale increases the mixed patch meandering, suggesting that the rim current instability contributes to the IOV of DWF.

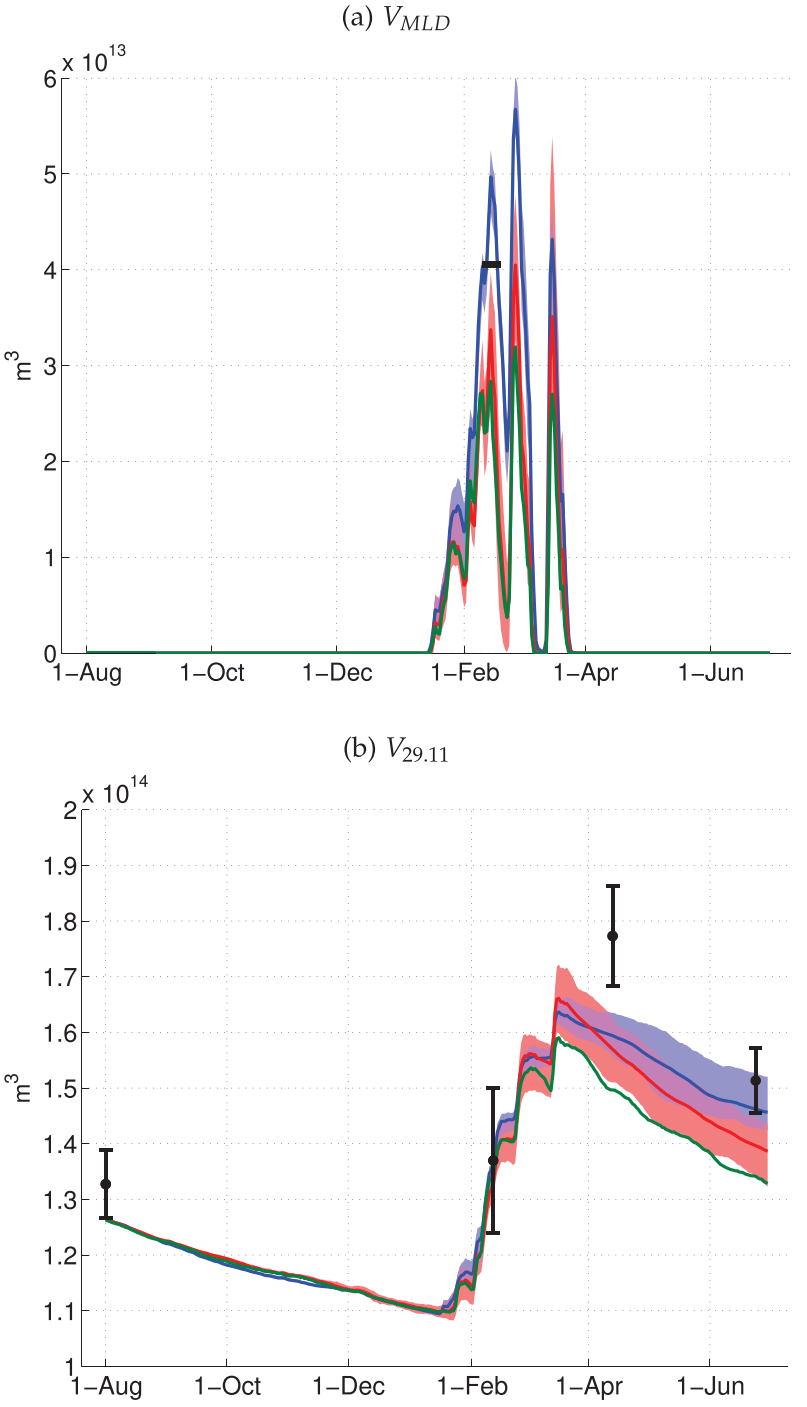

Figure 5. (a) Time series of the mixed patch volume V_{MLD} (MLD > 1,000 m) in observations (black), NEMOMED12 (blue), NWMED36 (red) ensemble, and NWMED36 low-resolution bathymetry sensitivity experiment (green). (b) Time series of the dense water volume $V_{29.11}$ with the same color code; the observed 95% confidence interval (Waldman et al., 2016) is also displayed. In both simulation ensembles, the mean (bold line), and min-max (envelope) volumes are displayed.

We now examine the integrated DWF and restratification volume IOV (Figure 5 and Table 3). The annual maximum V_{MLD} and V_{dens} ensemble STD is increased by a factor, respectively, 3 and 2 with the mesoscale, reaching, respectively, 14% and 7%. The difference between both estimates might be related to the fact that V_{MLD} is more instantaneous than V_{dens} which integrates all intense mixing events over time and also

results from lateral processes (mixing and transport). As a consequence, the latter is less impacted by IOV. Finally, the IOV of $V_{Restrat}$ does not increase with the mesoscale, reaching 11% and suggesting that the mesoscale impacts more IOV during the intense mixing phase than the restratification phase.

To conclude, the mesoscale improves the representation of the 2012–2013 mixed patch extent in the NBF-W, NC, and L areas. It significantly reduces the DWF rate from late January to 10 February 2013, which is underestimated. Finally, the restratification rate is enhanced by the mesoscale, in better agreement with observations. Both results regarding the mean DWF inhibition and restratification enhancement are in agreement with results from Herrmann et al. (2008). They also found a large DWF reduction in the NBF-W area. The mesoscale was shown to increase the mixed patch DF and most simulated DWF areas are impacted by IOV. In addition, the mixed patch circumference is increased, suggesting that its rim current meanders contribute to the IOV of DWF. Finally, the ensemble standard deviation of the annual maximum DWF rate increases from 3% to 5% at eddy-permitting resolution to 7–14% at eddy-resolving resolution. Therefore, the mesoscale increases by a factor 2–3 the intrinsic variability of DWF rates, which however remains modest. This is in qualitative agreement with Waldman et al. (2017) who showed that IOV impacts mostly DWF geography but only marginally the integral DWF rate. Such an impact is likely to be increased at the interannual time scale.

4. Causes of the Mesoscale Impact on Dense Water Formation

4.1. Mean Impact

4.1.1. Diapycnal Water Mass Transformations

In the previous section, we found during the intense mixing phase a discrepancy between the significant V_{MLD} decrease by the mesoscale in the 11 February 2012 to 28 February 2013 period and as an annual maximum and the insignificant impact on V_{dens} in the same periods. In addition, $V_{29.11}$ showed a significant restratification volume increase related to the mesoscale. Here we compute a water mass transformation diagnostic as a function of σ_0 (Tziperman & Speer, 1994) to investigate the robustness and cause of those effects. Figure 6 displays the water mass transformation diagnostic in both simulation ensembles, for the three phases of DWF. The preconditioning phase (Figures 6a, 6d, 6g, 6j) is dominated at both resolutions by the replacement of WMDW denser than 29.102 $\mathrm{kg/m^3}$ by lighter water, mostly (80–90%) Levantine Intermediate Waters (LIW) of density 29.08−29.10 $\mathrm{kg/m^3}$. The corresponding DT is deduced from the largest diapycnal volume transformation as a function of density that occurs during this phase. It reaches $-2.4\pm0.0\times10^{13}$ $\mathrm{m^3}$ for NEMOMED12 and it is little but significantly higher, reaching $-2.6\pm0.1\times10^{13}$ $\mathrm{m^3}$, for NWMED36. The lateral transport T largely dominates the dense water budget in this phase, whereas both surface formation and interior mixing are at least one order of magnitude lower for dense waters. T is driven by the meridional exchanges with the Algerian basin between Menorca and Sardinia islands. As a consequence, during preconditioning, the mesoscale enhances marginally meridional exchanges between the NWMed and Algerian basins, increasing the export of WMDW and the import of LIW.

During the intense mixing phase, Figures 6b, 6e, 6h, 6k show at both resolutions a large dense water formation with a DT of 5.8 ± 0.2 and $5.5\pm0.4\times10^{13}$ $\mathrm{m^3}$, respectively, for NEMOMED12 and NWMED36. However, the difference is not significant, which confirms results from Figure 5b. Therefore, the DWF volume estimates based on the mixed patch volume and on diapycnal transformations are not equivalent. The dense waters formed are significantly denser in NEMOMED12, between 29.114 and 29.128 $\mathrm{kg/m^3}$, as compared to 29.112 and 29.122 $\mathrm{kg/m^3}$ with NWMED36. It means that although the volume of dense waters formed is equivalent at both resolutions, their densification is inhibited by the mesoscale, mostly through a reduction of the WMDW cooling. It is consistent with the V_{MLD} reduction in Figure 5a which indicates that dense waters have been subjected to surface cooling for a shorter time with the mesoscale. At both resolutions, most of the DWF is associated with the destruction of lighter WMDW, as ∼65% of the water destroyed has $29.10 < \sigma_0 < 29.114$ $\mathrm{kg/m^3}$.

The dominant physical contribution to this densification is the surface forcing Su, and its magnitude is significantly higher with mesoscale, reaching a maximum of, respectively, 6.4 and 7.0×10^{13} $\mathrm{m^3}$ in NEMOMED12 and NWMED36. At the same time, the interior mixing is also significantly larger with mesoscale, reaching a maximum of, respectively, 3.5 and 4.5×10^{13} $\mathrm{m^3}$ in NEMOMED12 and NWMED36. This result contradicts former results by Herrmann et al. (2008). However as argued before their model configurations do

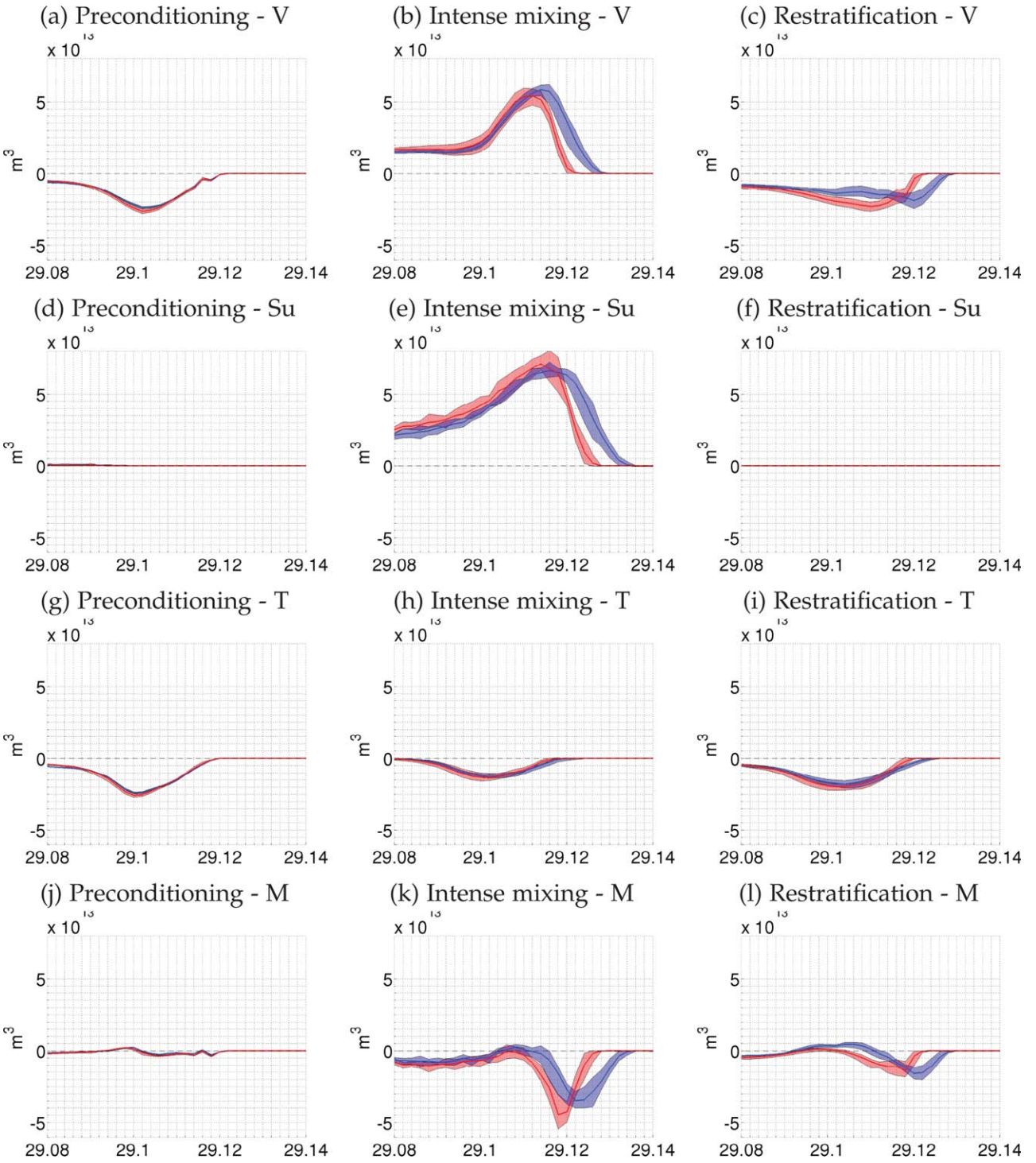

Figure 6. (a–c) NWMed Sea dense water volume (V) variation ($\times 10^{13}$ m^3) as a function of σ_0 in the three phases of convection: preconditioning (1 August 2012 to 4 January 2013), intense mixing (5 January 2013 to 24 March 2013) and restratification (25 March 2013 to 30 June 2013) in NEMOMED12 (blue) and NWMED36 (red) ensembles. The bold lines represent the ensemble mean and the envelopes cover minimum and maximum values. (d–f), (g–i), and (j–l): contributions for all three periods of, respectively, surface fluxes (*Su*), lateral transport (*T*), and internal mixing (*M*).

not differ only in terms of horizontal resolution, so that their models' different behaviors are not exclusively due to resolution. Both contributions occur at lower densities with the mesoscale, in agreement with the lower WMDW densification with mesoscale. *Su* is maximum at, respectively, 29.116 and 29.112 kg/m^3 in

NEMOMED12 and NWMED36, and *M* is maximum at, respectively, 29.118 and 29.122 kg/m^3. Therefore, the insignificant impact of the mesoscale on the intense mixing phase DT is the result of an increased surface formation compensated by an increased internal mixing. A comparison between the spatial structures of *Su* at both resolutions (not shown) reveals that it is largely increased with the mesoscale in the northern edge of the NBF-W area whereas it is decreased to the south of it. This suggests that the decreased DWF in the NBF-W area with the mesoscale maintains for a longer period waters of SSρ=29.11 kg/m^3, which causes an increase of *Su* at this isopycnal level. In addition, the decreased DWF in the NBF-W area also originates from the presence of lower density waters in this area which increase *M* during the intense mixing phase. Also, the larger mixed patch meandering with the mesoscale quantified in Table 3 might contribute to the *M* increase during DWF as it increases the surface of contact between the new WMDW and the lighter surrounding waters. Finally, *T* resembles highly its structure during preconditioning, it has a small contribution to diapycnal transformations in the intense mixing phase and it is not significantly impacted by the mesoscale.

During the restratification phase, Figure 6c shows that the DT is significantly higher with mesoscale, in agreement with results from Figure 5b: it reaches respectively -1.9 ± 0.2 and $-2.3\pm0.2\times10^{13}$ m^3 for NEMOMED12 and NWMED36. Dense water transformations occur at lower densities with mesoscale: the waters destroyed have densities of, respectively, 29.120−29.128 and 29.110−29.122 in NEMOMED12 and NWMED36. It corresponds to the densities of the new WMDW formed during the intense mixing phase. In both cases, the waters formed have properties of AW, LIW, and lighter WMDW, however, the formation of LIW and lighter WMDW is higher with mesoscale. *M* dominates the impact of the mesoscale on the restratification phase (Figures 6f, 6i, and 6l). Indeed, *Su* is negligeable by construction and *T* is not significantly increased with mesoscale, although the incoming LIW and outcoming WMDW are lighter. At both resolutions, *M* destroys mostly the densest WMDW and partly LIW to form WMDW of intermediate density. However, the magnitude of transformations and the density of the WMDW transformations are significantly lower with mesoscale. This might be the consequence of smaller density gradients within the WMDW layer in NWMED36, as a consequence of the smaller WMDW densification during the intense mixing phase. Therefore, the mesoscale decreases the internal mixing but it increases diapycnal transformations during the restratification phase. This apparent paradox is explained by the fact that *T* and *M* compensate in NEMOMED12, the former exporting most of the WMDW formed by the latter, which is true to a lesser extent for NWMED36. Finally, results regarding transport are in disagreement with Herrmann et al. (2008), whereas those regarding internal mixing agree with their study.

4.1.2. Mean Circulation and Stratification

We now aim at interpreting the significant impacts of the mesoscale on the areas NBF-W, NC, NBF-E, and L, which caused an average reduction of the V_{MLD} in the 10 February 2013 to 19 February 2013 period and of its annual maximum. For that, Figure 7 displays the time average velocities at 50 m depth $\mathbf{u_{50}}$ in NWMED36 for the period 1 August 2012 to 30 June 2013 and their difference with respect to NEMOMED12. As several dynamical structures in the NWMed Sea such as the NC are surface-intensified (Crépon et al., 1982), $\mathbf{u_{50}}$ is relevant to diagnose the mean basin-scale circulation below the Ekman layer which dominates the lateral advection of buoyant AW to the DWF area. In Figure 7a, we note that in NWMED36, the most energetic mean circulation is the NC and boundary currents off the Balearic, Corsica, and Sardinia islands. Mean velocities reach up to 15 cm/s off Sardinia, 20 cm/s off Corsica, 25 cm/s off Menorca, and 50 cm/s in the NC. Those boundary currents are narrow (∼50 km) and their core is close to the coast (∼20 km). In the open-sea, mean velocities are below 10 cm/s. We identify a mean meandering circulation with velocities higher than 5 cm/s resulting from the NBF. It flows north from (40°N, 5.2°E) to (41.5°N, 4.5°E), then southeast until (40.5°N, 5.5°E) and finally northeast until (42°N, 7°E). NC area is located in the southern edge of the NC, NBF-W and NBF-E area are crossed by the NBF and L is crossed by no mean current.

Figure 7b displays time mean differences between NWMED36 and NEMOMED12 simulations. The main impact of the mesoscale on the basin-scale circulation is a significant intensification of all boundary currents. Velocities are increased by up to 5 cm/s off Corsica, 7.5 cm/s off Sardinia, 12.5 cm/s off Menorca, and 20 cm/s in the NC. In addition, the mesoscale also narrows boundary currents. As a consequence, the NC area is significantly impacted by a weakening of the NC. As the NC carries light Atlantic Waters (AW) to the basin, such a reduction might explain the DWF increase in the NC area. Offshore, mean currents are weaker and highly impacted by the NBF instability (Escudier et al., 2013), therefore, most of the mesoscale impact

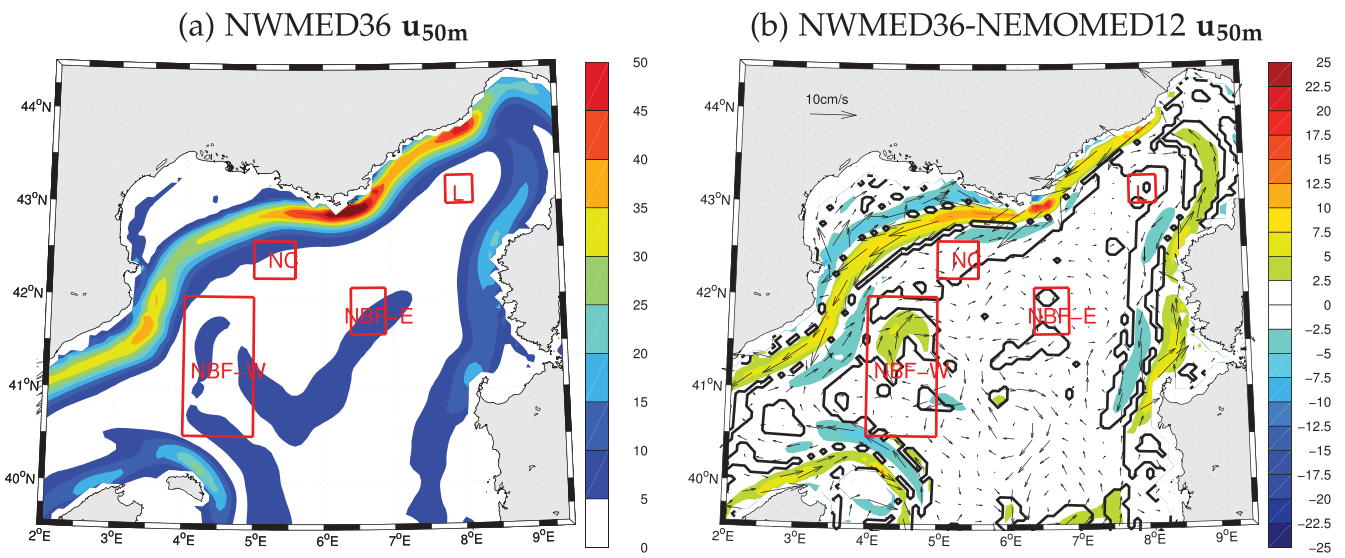

Figure 7. (a) NWMED36 time mean velocities at 50 m depth ($\mathbf{u_{50}}$, cm/s) and their module ($|\mathbf{u_{50}}|$) for the period 1 August 2012 to 30 June 2013. (b) NWMED36 time mean u_{50} anomaly map with respect to NEMOMED12. The black contour displays the 99% significance level (Student's *t* test, two-sided) for ensemble mean differences. The four areas where dense water formation differs are displayed in red: the Northern Current (NC), Western (NBF-W) and Eastern (NBF-E) North Balearic Front, and the Ligurian Sea (L).

on mean circulation is insignificant. It is the case in the NBF-E and L areas. However, the north of the NBF-W area shows a significant increase of the cyclonic circulation with mesoscale, with velocity increases by 2.5–5 cm/s. It is of the same magnitude as the NBF meander identified in Figure 7a, which means that without mesoscale, such a mean meander is not present. This meander carries light AW to the DWF area, and its presence with mesoscale might explain the DWF decrease in the NBF-W area.

In order to relate subsurface circulation anomalies to stratification anomalies, Figure 8a displays the mean bottom IS in NWMED36 for the period 1 August 2012 to 30 June 2013 and its anomaly with respect to NEMOMED12. It measures the integral buoyancy of the water column. Waldman et al. (2017) have shown that

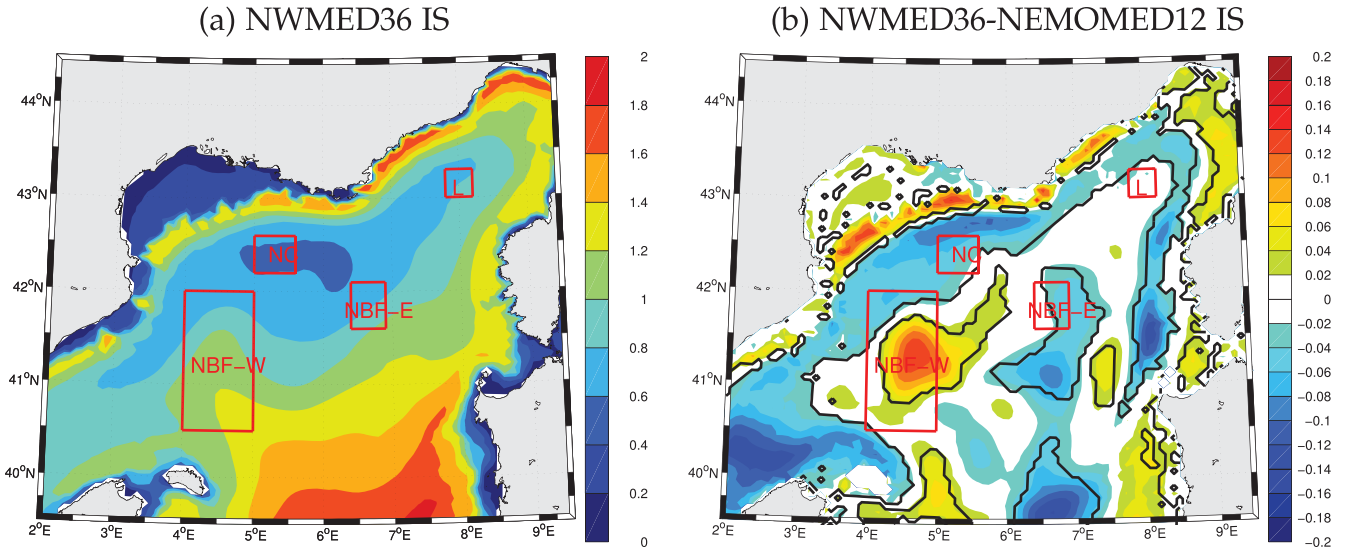

Figure 8. (a) NWMED36 time mean bottom Index of Stratification (IS, m^2/s^2) for the period 1 August 2012 to 30 June 2013. (b) NWMED36 time mean bottom IS anomaly map with respect to NEMOMED12. The black contour displays the 99% significance level (Student's *t* test, two sided) for ensemble mean differences. The areas where dense water formation differs are displayed in red: the Northern Current (NC), Western (NBF-W) and Eastern (NBF-E) North Balearic Front, and the Ligurian Sea (L).

70% of the NWMed Sea bottom IS on 1 August 2012 is due to the AW layer between 0 and 200 m depth. Therefore, we interpret the bottom IS spatial structures in Figure 8 in relation to the near-surface circulation $\mathbf{u_{50}}$. We see a mean meridional IS gradient that corresponds to a gradient between cold and salty (dense) AW in the NWMed and warm and fresh (light) AW in the Algerian basin. The high IS gradient area corresponds to the NBF. We identify its northward meander in the NBF-W area and its signature in the NBF-E area. In addition, an IS maximum is present at the periphery of the NWMed Sea, which corresponds to the circulation of light AW within boundary currents. The northern edge of the NC area is impacted by the positive IS anomaly due to the boundary current narrowing. To the center of the NWMed Sea, a minimum IS is present, which identifies the general cyclonic basin-scale circulation and the DWF area. Indeed, the doming of isopycnals in the DWF area is associated with high density (equivalent to low buoyancy) anomalies which cause the low IS. Finally, shelf areas show very low ($<0.4\,m^2/s^2$) bottom IS which are due to the low water column depth.

Figure 8b displays the mean bottom IS anomaly between both simulation ensembles. Most of the boundary current areas are significantly impacted by mesoscale in terms of stratification. To the offshore side of the Corsica, Ligurian, Mallorca, Menorca boundary currents, and of the NC, the mesoscale decreases the mean IS. On the contrary, to the onshore side of the Corsica, Ligurian boundary currents and the NC, the mesoscale increases the mean IS. As boundary currents are intensified with mesoscale, it means that isopycnal slopes are steeper. As a consequence, the AW layer depth is decreased offshore, and increased onshore, which creates a dipolar IS anomaly. This leads in particular to a significant IS decrease in the NC area, which is consistent with the DWF increase. We also note a significant IS decrease to the northern edge of the NBF-W area related to the NC relocation, which is inconsistent with the DWF decrease (Figure 4a). In addition, the mean IS is significantly impacted by the mesoscale along the NBF: it is increased to the west, in an area centered in the NBF-W area, and it is reduced to the east at the vicinity of the NBF-E area. The former is consistent with a meander in the NBF-W area only present with mesoscale, whereas the latter is associated with no significant circulation feature (Figure 7b). The NBF-W area is significantly impacted by the IS increase, whereas the NBF-E area shows no significant impact. In addition, L area shows no significant impact of the mesoscale on IS. Finally, we note a large IS decrease due to the mesoscale in the Balearic Sea, which is partly consistent with the boundary currents onshore relocation.

4.1.3. Buoyancy Budget in the Areas Impacted by the Mesoscale

Mean circulation and buoyancy features have permitted to interpret the mean impact of the mesoscale on DWF in the NC and NBF-W areas. However, the significant DWF increase in the NBF-E area and its decrease in the L area remain to be interpreted. In addition, the northern edge of the NBF-W area shows a mean IS decrease with mesoscale, which is inconsistent with the DWF decrease visible in Figure 4a. Therefore, we aim at quantifying the daily IS anomaly evolution between both simulation ensembles. Following Estournel et al. (2016), we assume σ_0 is constant at the ocean bed, which is mostly true even during DWF (see Figure 6b), which implies that the IS anomaly only depends on integral surface forcing and lateral advection anomalies (providing cabbelling is neglected and lateral mixing is purely isopycnal). At both resolutions, the surface forcing ALDERA is identical and the SST restoration impacts marginally the buoyancy flux anomaly (not shown). Therefore, we interpret in the following that the impact of the mesoscale on the bottom IS is solely related to horizontal advection.

Figure 9 displays the IS anomaly time series between both models at the NC, NBF-W, NBF-E, and L areas (location in Figure 7) as well as in the ensemble mean integrated DWF area. In all areas impacted by the mesoscale (Figures 9a–9d), the IS anomaly has a large high-frequency variability that develops from early September 2012, that is after typically 30–45 days of simulation. The NC area is marked most of the year with a significant negative IS anomaly in agreement with its 2012–2013 mean (Figure 8b). However, the NBF-W, NBF-E, and L areas have insignificant IS anomalies most of the year, which is consistent with the insignificant yearly mean anomaly for NBF-E and L, but inconsistent with the significant positive yearly mean IS anomaly in the NBF-W area (Figure 8b).

The NC area experiences significant IS anomalies with mesoscale throughout the simulation and particularly in the period from 10 January 2013 to 3 June 2013. Therefore, we conclude that in the NC area, high-frequency lateral buoyancy advection impacts marginally the mean IS decrease signal induced by the mesoscale. On the contrary, the NBF-W area only shows positive IS anomalies related to the mesoscale in the winter, between 25 January 2013 and 10 March 2013. They are insignificant the rest of the year except from the 25 November 2012 to 30 November 2012 period. The IS anomaly therefore largely impacts DWF, but high-frequency IS advection anomalies dominate over the mean IS increase most of the year in this area. It might

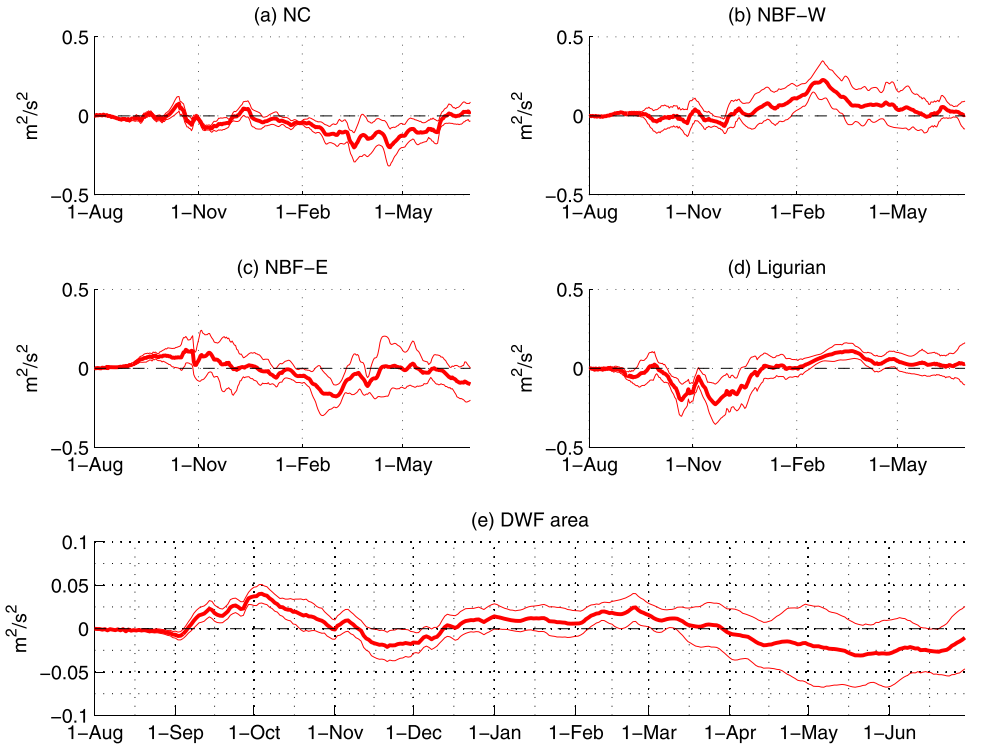

Figure 9. Bottom Index of Stratification (IS, m^2/s^2) anomaly between NWMED36 and NEMOMED12 in the areas of dense water formation (DWF) difference (a) Northern Current (NC), (b) North-Balearic Front—West (NBF-W), (c) North Balearic Front—East (NBF-E), (d) Ligurian Sea (L), and (e) in the modeled DWF area. The modeled DWF area includes the ensemble mean DWF area of both NEMOMED12 and NWMED36 ensembles. The bold and thin lines represent the ensemble mean and its 99% confidence interval (Student's *t* test, two sided).

be related to the large eddy activity related to the NBF (Escudier et al., 2013; Millot, 1999) or to a seasonal signature of its western meander. The NBF-E and L areas were shown to have no significant impact of the mesoscale on the mean IS. However, they both show over short periods significant IS anomalies, either positive or negative. The negative one between 25 January 2013 and 10 March 2013 explains the DWF increase in NBF-E area, and the positive one between 10 February 2013 and 5 April 2013 explains the DWF decrease in L area.

4.1.4. Does the Mesoscale Increase the DWF Area Stratification?

Finally, we look at a possible time-integral buoyancy convergence trend in the DWF area induced by the mesoscale, as expected from the baroclinic instability theory and from idealized modeling studies (Marshall & Schott, 1999). Figure 9e displays the IS difference between both models over the DWF area. It includes the area where DWF occurs in either model ensemble mean (bold contours in Figure 4b). As mentioned above, the IS anomaly between both simulations is dominated by lateral advection. It has values lower than 0.01 m^2/s^2 until early September. It experiences a significant positive anomaly in the 10 September 2012 to 16 October 2012 period, then a negative one in the 13 November 2012 to 3 December 2012 and finally a significant positive one in the 4 February 2013 to 1 March 2013 period, and it is insignificant the rest of the year. In particular, no significant linear IS trend appears in the 2012–2013 period, meaning that we identified no buoyancy increase trend resulting from mesoscale dynamics. The periods of significant positive IS anomaly are related to the NBF meander visible in Figure 7a and whose IS signature is visible in Figure 8b, although its location varies with time. The period of significantly negative IS anomaly is related to the NC anomaly visible in Figure 8b, although its location and magnitude along the NC also varies with time.

4.2. Impact on the Intrinsic Variability of Deep Convection

We now interpret the increase of intrinsic variability related to the mesoscale by quantifying and evaluating the modeled EKE at both resolutions in the NWMed Sea. Figure 10 displays (a) the mean EKE in NWMED36 between 1 August 2012 and 30 June 2013, (b) the EKE daily evolution in the Gulf of Lions from models and

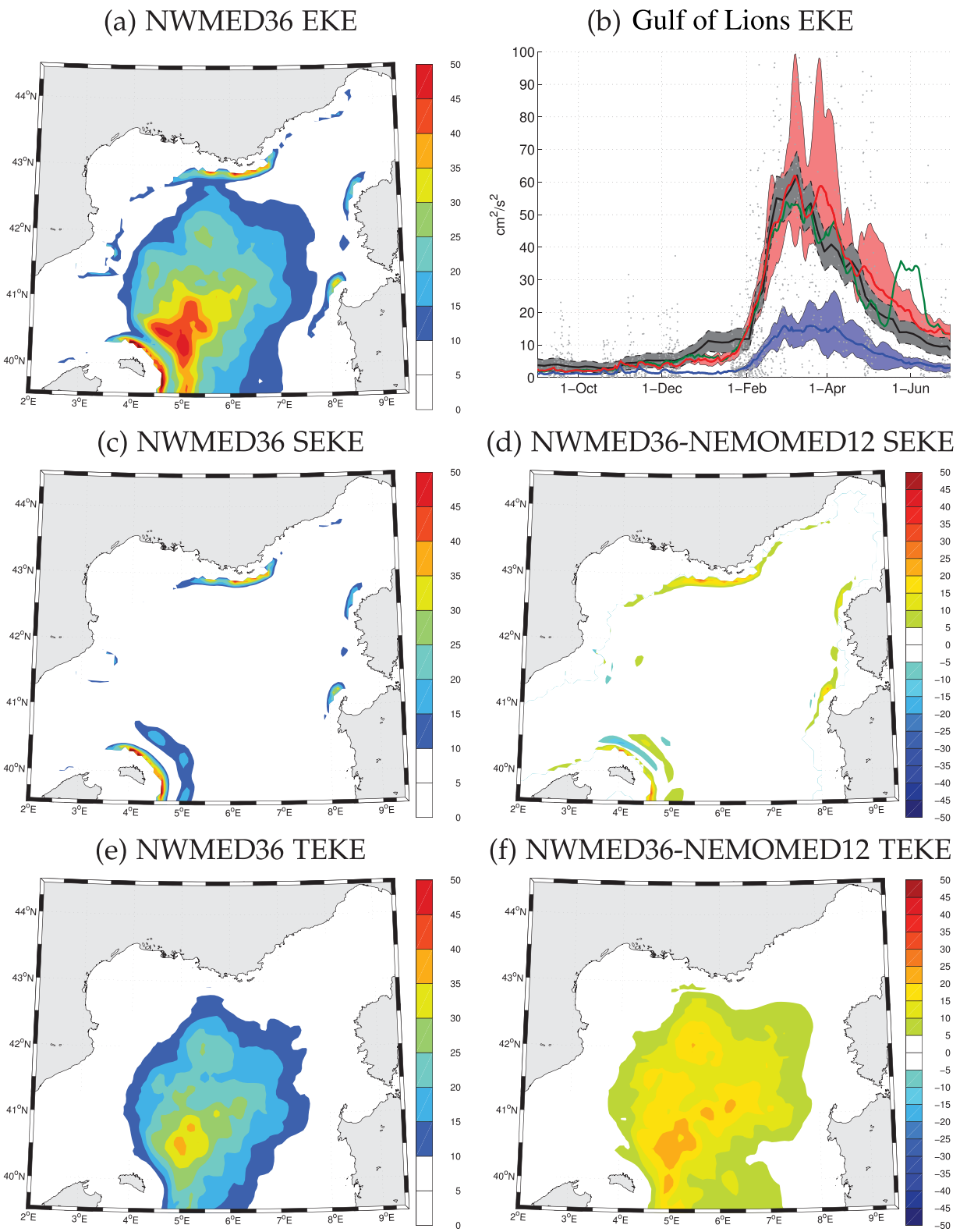

Figure 10. (a) NWMED36 averaged eddy kinetic energy (EKE, in cm^2/s^2) for the period 1 August 2012 to 30 June 2013. (b) Open-sea Gulf of Lions average ($4°E < lon < 6°E$, $lat > 41.25°N$, $H > 1{,}000$ m) EKE time series from observations (black), NEMOMED12 (blue), NWMED36 (red) ensemble mean (bold) and min-max (envelope) values and the NWMED36 low-resolution bathymetry sensitivity experiment (green). In observations, gray dots represent individual glider measurements, the black curve represents their 30 day running mean and the envelope displays its ensemble standard deviation. (c) NWMED36 time averaged standing EKE (SEKE) and (d) its anomaly with respect to NEMOMED12. (e and f) same as Figures 10c and 10d for the Transient EKE (TEKE).

glider observations, (c and e) NWMED36's mean SEKE and TEKE and (d and f) their anomaly with respect to NEMOMED12. We note two different patterns of mean EKE in NWMED36 simulation (Figure 10a): a large EKE at the boundary current location and also throughout the open-sea NWMed basin. The former reaches typically 15–45 cm^2/s^2 and is maximum off Menorca and in the NC, whereas the latter varies in the 10–50 cm^2/s^2 range and it is maximum to the southwest of the NBF. In NWMED36, the EKE is 95% larger than the MKE, meaning that most of the modeled NWMed Sea KE is at mesoscale. This result is consistent with global altimetry data showing from surface geostrophic currents that the mesoscale KE is larger than large-scale KE (Stammer & Wunsch, 1999; von Storch et al., 2012). It is also possibly related to the 11 month short simulation period marked with an intense DWF winter.

The observed Gulf of Lions EKE shows a large seasonal variability in the 2012–2013 period (Figure 10b): it is as low as $4.5\pm2.0\,cm^2/s^2$ during preconditioning (until 4 January 2013), it increases sharply to reach $31.7\pm4.9\,cm^2/s^2$ during the intense mixing phase (until 24 March 2013) and it then decreases to $23.0\pm4.4\,cm^2/s^2$ during restratification. Its annual mean reaches $17.7\pm3.6\,cm^2/s^2$. We note large high-frequency variability, especially during the intense mixing and restratification phases, related to a high velocity variability and possibly to spatial coverage. In both numerical simulation ensembles, the mean Gulf of Lions EKE reproduces qualitatively the sharp increase from early February and its slower decrease from late March. However, the annual mean EKE reaches, respectively, $5.0\pm0.6\,cm^2/s^2$ in NEMOMED12 and $17.3\pm1.5\,cm^2/s^2$ in NWMED36: the mesoscale therefore increases EKE by a factor 3.5, in largely better agreement with observations. Indeed, model bias dramatically decreases from −72% in NEMOMED12 to −2% in NWMED36. Therefore, the mesoscale largely improves the representation of eddy activity, which in turn enhances the intrinsic variability of DWF.

The EKE displays the mesoscale and smaller-scale KE ($L < 100$ km), however only transient mesoscale structures contribute to intrinsic variability. Therefore, we decompose the EKE into its standing component (SEKE) and its transient one (TEKE). The mean SEKE (Figure 10c) map partly resembles the $|\mathbf{u_{50}}|$ (Figure 7a): it reaches values larger than 10 cm^2/s^2 exclusively along the main boundary currents. No strong SEKE signature is visible in parts of those boundary currents and in the interior NWMed Sea, contrary to $|\mathbf{u_{50}}|$ (Figure 7a): indeed, they are surface-intensified and their contribution to the 0–1,000 m velocities is lower than more barotropic currents. Now anomalies due to the mesoscale (Figure 10d) are mostly positive, meaning that the mesoscale intensifies the boundary currents which are mostly stationary. Negative anomalies are found offshore Menorca boundary current, consistent with its narrowing visible in Figure 7b. The SEKE is increased on average by 41% with mesoscale in the open-sea ($H > 1,000$ m) NWMed basin.

Finally, the TEKE in NWMED36 (Figure 10e) reaches high values mostly in the open-sea, especially along and to the southwest of the NBF. It accounts for 70% of the total EKE and 46% of the NWMed Sea KE. This result means that in the NWMed Sea, approximately half of the KE originates from transient mesoscale eddies: therefore, they are a major component of the NWMed Sea circulation. In particular, most of the areas impacted by IOV (Figure 4b) are located in regions with a $TEKE > 10\,cm^2/s^2$ on average. Anomalies due to the mesoscale (Figure 10f) are positive throughout the NWMed Sea. They reach values higher than $15\,cm^2/s^2$ in a large fraction of the DWF area, especially in the NBF and around LION buoy. The TEKE is the component of the total KE which is mostly impacted by the mesoscale, with an increase factor of 2.9. It explains most (85%) of the EKE increase with mesoscale. This TEKE gives a physical rationale for the increase of intrinsic variability by mesoscale dynamics.

To conclude, water mass transformation diagnostics have confirmed the robustness of two results found in section 3: the mesoscale does not significantly impact integral dense water volume transformations during the intense mixing phase, but it significantly increases them during the restratification phase. The analysis of mean near-surface circulation and integral stratification has revealed two dominant effects of the mesoscale: the intensification and onshore relocation of all boundary currents which decreases the IS offshore, and the presence of a meander of the NBF in the NBF-W area associated with a positive IS anomaly. High-frequency lateral IS advection also impacts largely the IS anomaly and it contributes to the mean impact of the mesoscale on the DWF area. In addition, no significant buoyancy increase trend related to the mesoscale was identified, suggesting that a longer integration period is necessary to detect it. Finally, the NWMed Sea EKE is dramatically increased by the mesoscale, in far better agreement with observations, mostly due to the TEKE increase. It provides a physical interpretation to the increase in the intrinsic variability of DWF with mesoscale.

5. Discussions

5.1. Mean Mesoscale Impact on DWF

In this study, we have assessed the impact of the mesoscale dynamics exclusively by comparing two simulation ensembles only differing by their horizontal resolution. However, the mesoscale eddy size, which scales as the Rossby radius (Chelton et al., 2011), varies in time and space in the NWMed Sea, being higher in summer and to the south when and where buoyancy stratification is higher. Therefore, this study strictly focuses on dynamical structures of size between the effective resolution of NWMED36 (14.2–16.7 km) and that of NEMOMED12 (42.5–50 km). It excludes the impact of larger mesoscale structures (up to 80–100 km, Millot, 1991) on DWF as they are resolved at both resolutions. However, it can also include SCVs whose diameter is typically 15 km (Bosse et al., 2016) and which are permitted in NWMED36 model. The evaluation of the separate impacts of the mesoscale and submesoscale on DWF is not trivial and left for further studies.

Also, in NWMED36, both the horizontal dynamics and the bathymetry are at high-resolution. Therefore, either one can be responsible for the differences between both ensembles. We thus performed a twin simulation with the physical resolution of NWMED36 but with NEMOMED12 bathymetry resolution, and the initial state identical to one ensemble member. Figures 5 and 10b display in green its modeled deep convection volume V_{MLD}, its dense water volume $V_{29.11}$ and EKE daily time series. The modeled maximum convection volume is $V_{\mathrm{MLD}}=3.2\times 10^{13}\,\mathrm{m}^3$, the restratification volume is $V_{Restrat}=1.6\times 10^{13}\,\mathrm{m}^3$ and the time mean EKE is $\mathrm{EKE}=16.8\,\mathrm{cm}^2/\mathrm{s}^2$. Thus, with no high-resolution bathymetry, we obtain the same major response of DWF to mesoscale: a significantly lower mixed patch volume, stronger restratification rate, and large EKE increase, the two latter having no significant difference with the NWMED36 ensemble. We conclude that the impact of the mesoscale on deep convection occurs mainly through the oceanic internal physics, and not through its external forcing by high-resolution bathymetry.

We have found a mean mesoscale-related V_{MLD} reduction and $V_{Restrat}$ increase. Results were found to be related both to the impact of the mesoscale on mean circulation and stratification, and to its impact on high-frequency buoyancy advection. The impact of the mesoscale on mean circulation might be initial state-dependent. In particular, the high bottom IS related to the western NBF meander is visible on 1 August 2012 (Waldman et al., 2017), and it is initialized in the large-scale hydrology from Estournel et al. (2016). NWMED36 succeeds in reproducing this meander on average over the period 2012–2013, contrary to NEMOMED12. However, this meander might experience some long-term variability so that our results would not be necessarily true for another DWF year. However, the presence of a similar mixed patch anomaly in Herrmann et al. (2008) eddy-resolving model supports the hypothesis that such a pattern is stable.

In terms of water mass transformations, we showed that during the intense mixing phase internal mixing explains the lower densification of WMDW due to the mesoscale, and during the restratification phase it explains the increased restratification volume. However, this term is only deduced as a residual and therefore the physical and geographic sources of such a mixing cannot be determined. An explicit mixing computation would allow addressing this issue. In addition, two approximations were made which can impact our results: that the impact of solar heat flux penetration on the surface term is neglectable and that isoneutral can be approximated as isopycnals. The first approximation was shown to have large impacts on estimated water mass transformations (Bozec et al., 2008; Iudicone et al., 2008), however we only diagnose dense waters in this study, whose surface formation occur when the water column is homogeneous in the vertical so that solar penetration is unlikely to impact our results. The second approximation was shown to largely impact mixing estimates far from the surface on a global scale (Jackett & McDougall, 1997) but no neutral density function has been implemented so far in the Mediterranean Sea.

The question of the origin of the high-frequency buoyancy advection that impacts DWF at mesoscale remains open. We identified that this anomaly develops after typically 30–45 days of simulation. It corresponds both to the first strong wind event in the NWMed Sea which occurred after 30 days of simulation and to the characteristic time scale for the development of baroclinic instabilities (Estournel et al., 2016). Such a high-frequency impact might therefore result from a different response to the same wind forcing, in agreement with strong and small-scale frictional potential vorticity fluxes identified by Giordani et al. (2017), or from a different development of baroclinic instabilities at both resolutions.

Finally, we found no buoyancy convergence trend resulting from the mesoscale, contrary to predictions from baroclinic instability theory and idealized simulations (Marshall & Schott, 1999). This surprising result

might be due to the short integration time and to large individual eddy signatures on bottom IS, particularly in the north-Balearic front. In addition, the absence of such a signal might result from a compensation between an IS decrease due to mean circulation and an IS increase due to transient eddies.

5.2. Impact of the Mesoscale on the Intrinsic Ocean Variability

This study quantifies for the first time the impact of IOV on DWF in an eddy-resolving configuration. For this purpose, we perturbed the mesoscale hydrology in summer 2012, assuming that IOV is mostly related to mesoscale activity. Therefore, we made two approximations regarding the spatial scales involved: that smaller scales (e.g., submesoscale) and basin-scale hydrology play a marginal role in IOV. The former is unresolved by NEMOMED12 and only permitted in NWMED36 and to our knowledge, its impact on IOV has not been assessed so far: it remains an open question left for further studies.

Now the basin-scale hydrology was fixed in summer 2012 in order to reproduce realistically the 2012–2013 case study. By doing so, the large-scale IOV was canceled by observations. However, a recent study (Sérazin et al., 2015) suggests the large impact of IOV at scales up to $\sim$500 km, which is the approximate size of the NWMed Sea. Therefore, in an uninitialized configuration, the basin-scale IOV might contribute to increase the total IOV. This issue is intimately related to time scales as the reverse energy cascade between mesoscale and basin-scale IOV takes place at interannual time scales (Sérazin et al., 2015). We can expect an increase of IOV at interannual time scales as a result of this inverse cascade.

5.3. Applicability of Results to High-Latitude Dense Water Formation Regions

The role of the mesoscale dynamics in setting the properties of the DWF phenomenon has also been studied extensively at high-latitude dense water formation regions such as the Labrador (Chanut et al., 2008; Gelderloos et al., 2011; Katsman et al., 2004; Luo et al., 2014; Saenko et al., 2014) and Irminger (Paquin et al., 2016) Seas in the Subpolar North Atlantic. The main specificities of this study with respect to the above mentioned ones are: the unprecedented number of observations of a DWF event; the use of a multiresolution model comparison to document the mesoscale dynamics; the analysis of both the transient and standing mesoscale dynamics; and the assessment of the IOV associated with the mesoscale dynamics.

Several results from this study could also be valid in high-latitude DWF regions. We showed that the mesoscale impacts the standing dynamics by intensifying and relocating onshore the main boundary currents of the NWMed Sea, which enhances DWF in the vicinity of the Northern Current. Both the Labrador and Irminger Sea DWF areas are bounded by boundary currents (respectively, the Labrador, Saenko et al., 2014) and East Greenland Currents, Paquin et al., 2016) carrying buoyant water to those basins. Saenko et al. (2014) have shown that low-resolution ocean models tend to misrepresent their parametrized eddy buoyancy fluxes between the boundary current and the interior region. Isachsen (2011) argues that such a misrepresentation of parametrized eddy fluxes is likely due to the lack of any bathymetry slope stabilization effect in mesoscale eddy parmetrizations. In light of these results, it is likely that the mesoscale dynamics enhances DWF in the vicinity of the Labrador and East Greenland Current, respectively, in the Labrador and Irminger Seas.

This study identifies the role of transient mesoscale eddies in largely enhancing the Transient EKE, which we argue causes a large increase in the intrinsic variability of DWF. Although no ensemble simulation framework has been proposed so far to test the applicability of these results to high-latitude deep convection areas, several modeling studies suggest the role of IOV in setting the variability of DWF in the Labrador (Luo et al., 2014) and Weddell (De Lavergne et al., 2014) Seas. In the Labrador Sea, Luo et al. (2014) show with regional eddy-permitting simulations that the interannual variability of the incoming Eastern Greenland Current properties is responsible for a fraction of the deep convection interannual variability. Such a variability, impacting deep convection through the detachment of Irminger Rings off the West Greenland Current, is likely to be partly intrinsic. In the Weddell Sea, (De Lavergne et al., 2014) suggest a possible historical deep convection shutdown caused by global warming and their results support a control of the shutdown timing by intrinsic climate variability, which can be partly oceanic. We also show, as in Waldman et al. (2017), that the IOV of DWF is maximum to the Southeast and minimum to the Northwest of the modeled deep convection region. This suggests that the IOV of DWF might also be highest in the open-sea border of the high-latitude deep convection regions, and lowest in the vicinity of the respective boundary currents.

5.4. Relative Importance of Air-Sea Fluxes, Initial Conditions, and Mesoscale in Setting the Properties of DWF

Comparing the roles of air-sea fluxes, the oceanic mesoscale and oceanic initial conditions in driving deep convection is a fundamental question. Our study strongly supports the vision that the mesoscale dynamics is a secondary driver of deep convection whereas atmospheric forcing is the first-order factor. This conclusion goes in line with Herrmann et al.'s (2008) similar conclusion on the 1986–1987 winter, as well as results by Luo et al. (2014) regarding the interannual variability of deep convection in the Labrador Sea.

As for oceanic initial conditions, several studies have addressed the role of summer preconditioning in modulating the magnitude and properties of the intense 2004–2005 (Herrmann et al., 2010) and 2012–2013 (Léger et al., 2016) deep convection winters. They have concluded on the secondary role of ocean summer preconditioning with respect to atmospheric forcing. Our results further suggest that the mesoscale has a third-order role, even lower than that of oceanic initial conditions, in the light of its low impact on the DWF rate and properties.

5.5. Comparison of NEMOMED12 and NWMED36 With Other Numerical Simulations of the 2012–2013 Case Study

Winter 2012–2013 is a golden case study to evaluate deep convection in numerical models. Up to now, several other studies have simulated this convective winter but no model intercomparison has been proposed so far. They include forced (Estournel et al., 2016; Giordani et al., 2017; Léger et al., 2016; Waldman et al., 2016, 2017, and this study) and coupled (Lebeaupin Brossier et al., 2017; Somot et al., 2016) runs, at eddy-permitting (Somot et al., 2016; Waldman et al., 2016, 2017) or eddy-resolving (Estournel et al., 2016; Giordani et al., 2017; Lebeaupin Brossier et al., 2017; Léger et al., 2016; Waldman et al., 2016, and this study) resolutions, initialized in summer 2012 (Estournel et al., 2016; Giordani et al., 2017; Lebeaupin Brossier et al., 2017; Léger et al., 2016; Waldman et al., 2017, and this study) or not (Somot et al., 2016; Waldman et al., 2016). Up to now, we can only compare the simulated V_{dens} which has been quantified in all the aforementioned studies. From the comparison between the simulated V_{dens} and Waldman et al.'s (2016) estimation from observations, we can draw the following conclusions:

1. Runs which are not initialized in summer 2012 largely underestimate V_{dens} (Léger et al., 2016; Somot et al., 2016; Waldman et al., 2016, IM36 run), which is partly corrected by the initialization procedure (Waldman et al., 2016). In particular, all initialized simulations but Léger et al.'s (2016) IPSY run have V_{dens} biases lower than 30%, which validates the NEMOMED12 and NWMED36 runs presented in this study.
2. All numerical simulations but Léger et al.'s (2016) IMAP run underestimate V_{dens}. This could be due to a common model bias although Waldman et al. (2016) stress the sensitivity of their estimation to instrumental stability, which could cause part of this appearent bias.
3. No general impact of coupling and/or high-resolution modeling on V_{dens} emerges.

We also believe that a dedicated intercomparison study would be beneficial and could document other key characteristics of deep convection such as air-sea exchanges, summer 2012 preconditioning, the geography and chronology of deep convection or the properties of the new deep waters formed.

6. Conclusions

In order to investigate the impact of the mesoscale dynamics on the 2012–2013 dense water formation (DWF) winter in the northwestern Mediterranean (NWMed) sea, we have performed two ensemble numerical simulations with a perturbed initial state, respectively, at mesoscale-permitting (6.1–7.1 km) and mesoscale-resolving (2.0–2.4 km) resolutions but with an identical numerical core. We have examined the mean impact of the mesoscale and its impact on the intrinsic variability of DWF, and we have investigated the physical causes of such effects.

The mean impact of the mesoscale on DWF occurs mainly through the oceanic internal physics and not the high-resolution bathymetry. It was shown to be modest: it does not modify the chronology of the deep convective winter nor the volume of dense waters formed. It also impacts marginally the location of the mixed patch, which is at both resolutions located off the Gulf of Lions in an open-sea region centered at the vicinity of LION buoy location. However the resolution of the mesoscale reduces its extent to the west of the North Balearic Front and in the Ligurian Sea and increases it along the Northern Current. The maximum

mixed patch volume is significantly reduced from 5.7 ± 0.2 to $4.2 \pm 0.6 \times 10^{13}$ m^3. This leads to a modest reduction of the dense water densification by 0.004 kg/m^3. Finally, the spring restratification volume is enhanced from 1.4 ± 0.2 to $1.8 \pm 0.2 \times 10^{13}$ m^3 by the mesoscale dynamics. Both the mixed patch geography and the restratification rate are improved with respect to observations, whereas the mixed patch volume presents a higher bias. This latter bias could be due to a reduction of a bias compensation present in NEMOMED12 between a surface buoyancy flux overestimation and a buoyant hydrological bias.

We then turned to the causes of this mean impact of the mesoscale on DWF. Water mass transformation diagnostics have confirmed that the mesoscale does not significantly impact integral dense water volume transformations during the intense mixing phase, but it significantly increases them during the restatification phase. In the intense mixing phase, the mesoscale reduces the densification of the newly formed Western Mediterranean Deep Waters as a result of an increased internal mixing. In the restratification phase, the dense water restratification volume is increased because internal mixing occurs at lower densities as a consequence of the deep convection event. We conclude that the increased restratification volume with the mesoscale is not explained by an increase of internal mixing but by its shift to lower densities. The analysis of mean basin-scale circulation and integral stratification has revealed two dominant effects of the mesoscale: the intensification and onshore relocation of all boundary currents which decreases the Index of Stratification (IS) offshore them, and the presence of a meander to the west of the North Balearic Front associated with a positive IS anomaly. The former is consistent with the DWF increase in the Northern Current area, the latter is consistent with the DWF decrease in the North Balearic Front area. However, high-frequency (daily to monthly) lateral buoyancy advection also largely impacts DWF anomalies related to the mesoscale, in particular in the Ligurian Sea. Finally, the impact of the mesoscale on the DWF area integral stratification is insignificant in most of the 2012–2013 period as well as its trend over the period. This suggests that a longer integration period is necessary to detect such a restratification effect by the mesoscale in the DWF area.

The mesoscale was shown to increase the intrinsic variability of surface ocean hydrology but not of the mixed layer depth at LION buoy. However, 65% of the mixed patch area is impacted by intrinsic variability in the eddy-resolving ensemble, 38% larger than in the eddy-permitting ensemble, which means that intrinsic variability plays a major role in determining the geography of deep convection. In addition, the mixed patch circumference is increased by 15%, suggesting that its rim current meanders contribute to the intrinsic variability of DWF. Finally, the intrinsic variability of the annual maximum DWF volume remains low in this well-constrained case study although it is increased by a factor 2–3 with the mesoscale.

We related the impact of the mesoscale on the intrinsic variability of DWF to the generation of Eddy Kinetic Energy (EKE). The mesoscale dramatically increases the Gulf of Lions EKE from 5.0 ± 0.6 to 17.3 ± 1.5 cm^2/s^2 between eddy-permitting and eddy-resolving ensembles, in far better agreement with the observed estimate of 17.7 ± 3.6 cm^2/s^2, although its seasonal cycle is qualitatively captured at both resolutions. When the mesoscale is resolved, the EKE is larger than the mean kinetic energy and it is largely dominated by the Transient EKE which accounts for half of the NWMed Sea total kinetic energy. Regions of particularly high Transient EKE are found in the open-sea, and they cover most areas of high intrinsic DWF variability, providing a physical rationale for it.

Acknowledgments

This work is a contribution to the HyMeX program (*HYdrological cycle in the Mediterranean EXperiment*—www.hymex.org) through INSU-MISTRALS support and through the ASICS-MED project (Air-Sea Interaction and Coupling with Submesoscale structures in the MEDiterranean, ANR-2012-BS06-003). We would like to acknowledge the DT-INSU staff of the National Pool of Gliders for the gliders deployments. Captains, crew members of R/V Le Tethys II (INSU) and R/V Le Suroit (Ifremer), as well as scientists who participated in the MOOSE-GE and DEWEX cruises are also warmly thanked. Observational Support was provided by the French MISTRALS program (HyMeX and MERMeX components), the MOOSE project (AllEnvi-INSU long-term observatory, http://www.moose-network.fr), the French Bio-Argo project (CNES-TOSCA) and the French NAOS project (ANR J11R107-F), as well as by the FP7 EU projects GROOM (grant agreement 284321), PERSEUS (grant agreement 287600), and JERICO (grant agreement 262584), and the EGO-COST Action ES0904. The data used in this study are included in the references: Testor et al. (2012), Testor (2013), Testor et al. (2013), Conan (2013), and Taillandier (2014).

References

ARGO (2000). *ARGO float data and metadata from global data assembly centre (ARGO GDAC)*. Paris, France: Sea Scientific Open Data Publication. https://doi.org/10.17882/42182

Auger, P., Estournel, C., Ulses, C., Stemmann, L., Somot, S., & Diaz, F. (2014). Interannual control of plankton ecosystem in a deep convection area as inferred from a 30-year 3D modeling study: Winter mixing and prey/predator interactions in the NW Mediterranean. *Progress in Oceanography*, *124*, 12–27. https://doi.org/10.1016/j.pocean.2014.04.004

Balmaseda, M. A., Mogensen, K., & Weaver, A. T. (2013). Evaluation of the ECMWF ocean reanalysis system ORAS4. *Quarterly Journal of the Royal Meteorological Society*, *139*(674), 1132–1161.

Béranger, K., Drillet, Y., Houssais, M.-N., Testor, P., Bourdallé-Badie, R., Alhammoud, B., . . . Crépon, M. (2010). Impact of the spatial distribution of the atmospheric forcing on water mass formation in the Mediterranean Sea. *Journal of Geophysical Research*, *115*, C12041. https://doi.org/10.1029/2009JC005648

Beuvier, J., Béranger, K., Brossier, C. L., Somot, S., Sevault, F., Drillet, Y., . . . Lyard, F. (2012). Spreading of the Western Mediterranean Deep Water after winter 2005: Time scales and deep cyclone transport. *Journal of Geophysical Research*, *117*, C07022. https://doi.org/10.1029/2011JC007679

Biastoch, A., Boning, C., & Lutjeharms, J. (2008). Agulhas leakage dynamics affects decadal variability in Atlantic overturning circulation. *Nature*, *456*(7221), 489–492.

Bohme, L., & Send, U. (2005). Objective analyses of hydrographic data for referencing profiling float salinities in highly variable environments. *Deep Sea Research Part II: Topical Studies in Oceanography*, *52*, 651–664.

Bosse, A., Testor, P., Houpert, L., Damien, P., Prieur, L., Hayes, D., . . . & Mortier, L. (2016). Scales and dynamics of Submesoscale Coherent Vortices formed by deep convection in the northwestern Mediterranean Sea. *Journal of Geophysical Research: Oceans*, *121*, 7716–7742. https://doi.org/10.1002/2016JC012144

Bosse, A., Testor, P., Mortier, L., Prieur, L., Taillandier, V., D'ortenzio, F., & Coppola, L. (2015). Spreading of Levantine Intermediate Waters by submesoscale coherent vortices in the northwestern Mediterranean Sea as observed with gliders. *Journal of Geophysical Research: Oceans*, *120*, 1599–1622. https://doi.org/10.1002/2014JC010263

Bozec, A., Bouret-Aubertot, P., Iudicone, D., & Crépon, M. (2008). Impact of penetrative solar radiation on the diagnosis of water mass transformation in the Mediterranean Sea. *Journal of Geophysical Research*, *113*, C06012. https://doi.org/10.1029/2007JC004606

Caniaux, G., Prieur, L., Giordani, H., & Redelsperger, J.-L. (2017). An inverse method to derive surface fluxes from the closure of oceanic heat and water budgets: Application to the north-western Mediterranean Sea. *Journal of Geophysical Research: Oceans*, *122*, 2884–2908. https://doi.org/10.1002/2016JC012167

Chanut, J., Barnier, B., Large, W., Debreu, L., Penduff, T., Molines, J. M., & Mathiot, P. (2008). Mesoscale eddies in the Labrador Sea and their contribution to convection and restratification. *Journal of Physical Oceanography*, *38*(8), 1617–1643.

Chelton, D. B., Schlax, M. G., & Samelson, R. M. (2011). Global observations of nonlinear mesoscale eddies. *Progress in Oceanography*, *91*(2), 167–216. https://doi.org/10.1016/j.pocean.2011.01.002

Colin, J., Déqué, M., Radu, R., & Somot, S. (2010). Sensitivity study of heavy precipitation in limited area model climate simulations: Influence of the size of the domain and the use of the spectral nudging technique. *Tellus, Series A*, *62*, 591–604.

Conan, P. (2013). *DEWEX-MERMEX 2013 LEG2 cruise, le Suroit R/V* (technical report). Retrrieved from http://campagnes.flotteoceanographique.fr/campagnes/13020030/

Crépon, M., Wald, L., & Monget, J. M. (1982). Low-frequency waves in the Ligurian Sea during December 1977. *Journal of Geophysical Research*, *87*, 595–600. https://doi.org/10.1029/JC087iC01p00595

Debreu, L., Vouland, C., & Blayo, E. (2008). AGRIF: Adaptive grid refinement in Fortran. *Computers and Geosciences*, *34*(1), 8–13. https://doi.org/10.1016/j.cageo.2007.01.009

De Lavergne, C., Palter, J. B., Galbraith, E. D., Bernardello, R., & Marinov, I. (2014). Cessation of deep convection in the open Southern Ocean under anthropogenic climate change. *Nature Climate Change*, *4*(4), 278–282. https://doi.org/10.1038/nclimate2132

Demirov, E. K., & Pinardi, N. (2007). On the relationship between the water mass pathways and eddy variability in the Western Mediterranean Sea. *Journal of Geophysical Research*, *112*, C02024. https://doi.org/10.1029/2005JC003174

Djath, B., Melet, A., Verron, J., Molines, J.-M., Barnier, B., Gourdeau, L., & Debreu, L. (2014a). A 1/36 degrees model of the Solomon Sea embedded into a global ocean model: On the setting up of an interactive open boundary nested model system. *Journal of Operational Oceanography*, *7*(1), 34–46.

Djath, B., Verron, J., Melet, A., Gourdeau, L., Barnier, B., & Molines, J.-M. (2014b). Multiscale dynamical analysis of a high-resolution numerical model simulation of the Solomon Sea circulation. *Journal of Geophysical Research: Oceans*, *119*, 6286–6304. https://doi.org/10.1002/2013JC009695

D'Ortenzio, F., Lavigne, H., Besson, F., Claustre, H., Coppola, L., Garcia, N., . . . Testor, P. (2014). Observing mixed layer depth, nitrate and chlorophyll concentrations in the northwestern Mediterranean: A combined satellite and NO_3 profiling floats experiment. *Geophysical Research Letters*, *41*, 6443–6451. https://doi.org/doi:10.1002/2014GL061020

Dufour, C. O., Le Sommer, J., Zika, J. D., Gehlen, M., Orr, J. C., Mathiot, P., & Barnier, B. (2012). Standing and transient eddies in the response of the Southern Ocean meridional overturning to the southern annular mode. *Journal of Climate*, *25*(20), 6958–6974.

Durrieu de Madron, X., Houpert, L., Puig, P., Sanchez-Vidal, A., Testor, P., Bosse, A., . . . Raimbault, P. (2013). Interaction of dense shelf water cascading and open-sea convection in the northwestern Mediterranean during winter 2012. *Geophysical Research Letters*, *40*, 1379–1385. https://doi.org/10.1002/grl.50331

Escudier, R., Bouffard, J., Pascual, A., Poulain, P.-M., & Pujol, M.-I. (2013). Improvement of coastal and mesoscale observation from space: Application to the northwestern Mediterranean Sea. *Geophysical Research Letters*, *40*, 2148–2153, https://doi.org/10.1002/grl.50324

Estournel, C., Testor, P., Damien, P., D'ortenzio, F., Marsaleix, P., Conan, P., . . . Prieur, L. (2016). High resolution modelling of dense water formation in the north-western Mediterranean during winter 2012–2013: Processes and budget. *Journal of Geophysical Research: Oceans*, *121*, 5367–5392. https://doi.org/10.1002/2016JC011935

Fairall, C., Bradley, E. F., Hare, J., Grachev, A., & Edson, J. (2003). Bulk parameterization of air-sea fluxes: Updates and verification for the COARE algorithm. *Journal of Climate*, *16*(4), 571–591.

Gaspar, P., Gregoris, Y., & Lefèvre, J. (1990). A simple eddy kinetic energy model for simulations of the oceanic vertical mixing: Tests at station Papa and long-term upper ocean study site. *Journal of Geophysical Research*, *95*, 16,179–16,193.

Gelderloos, R., Katsman, C. A., & Drijfhout, S. S. (2011). Assessing the roles of three eddy types in restratifying the Labrador Sea after deep convection. *Journal of Physical Oceanography*, *41*(11), 2102–2119.

Gent, P., & McWilliams, J. (1990). Isopycnal mixing in ocean circulation models. *Journal of Physical Oceanography*, *20*, 150–155.

Giordani, H., Lebeaupin-Brossier, C., Lger, F., & Caniaux, G. (2017). A PV-approach for dense water formation along fronts: Application to the Northwestern Mediterranean. *Journal of Geophysical Research: Oceans*, *122*, 995–1015. https://doi.org/10.1002/2016JC012019

Grégorio, S., Penduff, T., Sérazin, G., Molines, J.-M., Barnier, B., & Hirschi, J. (2015). Intrinsic variability of the Atlantic Meridional Overturning Circulation at interannual-to-multidecadal time scales. *Journal of Physical Oceanography*, *45*(7), 1929–1946.

Grignon, L., Smeed, D. A., Bryden, H. L., & Schroeder, K. (2010). Importance of the variability of hydrographic preconditioning for deep convection in the gulf of lion, NW Mediterranean. *Ocean Science*, *6*(2), 573–586. https://doi.org/10.5194/os-6-573-2010

Hamon, M., Beuvier, J., Somot, S., Lellouche, J.-M., Greiner, E., Jordà, G., . . . Drillet, Y. (2016). Design and validation of MEDRYS, a Mediterranean Sea reanalysis over the period 1992–2013. *Ocean Science*, *12*(2), 577–599. https://doi.org/10.5194/os-12-577-2016

Herrmann, M., Auger, P.-A., Ulses, C., & Estournel, C. (2017). Long-term monitoring of ocean deep convection using multisensors altimetry and ocean color satellite data. *Journal of Geophysical Research: Oceans*, *122*, 1457–1475. https://doi.org/10.1002/2016JC011833

Herrmann, M., Estournel, C., Diaz, F., & Adloff, F. (2014). Impact of climate change on the Northwestern Mediterranean Sea pelagic planktonic ecosystem and associated carbon cycle. *Journal of Geophysical Research: Oceans*, *119*, 5815–5836. https://doi.org/10.1002/2014JC010016

Herrmann, M., Sevault, F., Beuvier, J., & Somot, S. (2010). What induced the exceptional 2005 convection event in the northwestern Mediterranean basin? Answers from a modeling study. *Journal of Geophysical Reserach*, *115*, C08029. https://doi.org/10.1029/2009JC005749

Herrmann, M., & Somot, S. (2008). Relevance of ERA40 dynamical downscaling for modeling deep convection in the Mediterranean Sea. *Geophysical Research Letters*, *35*, L04607. https://doi.org/10.1029/2007GL032442

Herrmann, M., Somot, S., Calmanti, S., Dubois, C., & Sevault, F. (2011). Representation of spatial and temporal variability of daily wind speed and of intense wind events over the Mediterranean Sea using dynamical downscaling: Impact of the regional climate model configuration. *Natural Hazards and Earth System Sciences*, *11*, 1983–2001. https://doi.org/10.5194/nhess-11-1983-2011

Herrmann, M., Somot, S., Sevault, F., Estournel, C., & Déqué, M. (2008). Modeling the deep convection in the Northwestern Mediterranean sea using an eddy-permitting and an eddy-resolving model: Case study of winter 1986–87. *Journal of Geophysical Research*, *113*, C04011. https://doi.org/10.1029/2006JC003991

Houpert, L., Durrieu de Madron, X., Testor, P., Bosse, A., D'ortenzio, F., Bouin, M., . . . Raimbault, P. (2016). Observations of open-ocean deep convection in the northwestern Mediterranean Sea: Seasonal and interannual variability of mixing and deep water masses for the 2007–2013 period. *Journal of Geophysical Research: Oceans*, *121*, 8139–8171. https://doi.org/10.1002/2016JC011857

Isachsen, P. E. (2011). Baroclinic instability and eddy tracer transport across sloping bottom topography: How well does a modified Eady model do in primitive equation simulations? *Ocean Modelling*, *39*(1–2), 183–199. https://doi.org/10.1016/j.ocemod.2010.09.007

Iudicone, D., Madec, G., & McDougall, T. J. (2008). Water-mass transformations in a neutral density framework and the key role of light penetration. *Journal of Physical Oceanography*, *38*(7), 1357–1376. https://doi.org/10.1175/2007JPO3464.1

Jackett, D. R., & McDougall, T. J. (1997). A neutral density variable for the world's oceans. *Journal of Physical Oceanography*, *27*(2), 237–263.

Jouanno, J., Sheinbaum, J., Barnier, B., Molines, J. M., & Candela, J. (2012). Seasonal and Interannual Modulation of the Eddy Kinetic Energy in the Caribbean Sea. *Journal of Physical Oceanography*, *42*(11), 2041–2055. https://doi.org/10.1175/JPO-D-12-048.1

Katsman, C. A., Spall, M. A., & Pickart, R. S. (2004). Boundary current eddies and their role in the restratification of the Labrador Sea. *Journal of Physical Oceanography*, *34*(9), 1967–1983.

Leaman, K. D., & Schott, F. (1991). Hydrographic structure of the convection regime in the Gulf of Lions: Winter 1987. *Journal of Physical Oceanography*, *21*, 575–597.

Lebeaupin Brossier, C., Léger, F., Giordani, H., Beuvier, J., Bouin, M.-N., Ducrocq, V., & Fourrié, N. (2017), Dense Water Formation in the North-Western Mediterranean area during HyMeX-SOP2 in 1/36° ocean simulations: Ocean-atmosphere coupling impact. *Journal of Geophysical Research: Oceans*, *122*, 5749–5773. https://doi.org/10.1002/2016JC012526

Léger, F., Lebeaupin Brossier, C., Giordani, H., Arsouze, T., Beuvier, J., Bouin, M.-N., . . . Nuret, M. (2016). Dense water formation in the north-western Mediterranean area during HyMeX-SOP2 in 1/36° ocean simulations: Sensitivity to initial conditions. *Journal of Geophysical Research: Oceans*, *121*, 5549–5569. https://doi.org/10.1002/2015JC011542

L'Hévéder, B., Li, L., Sevault, F., & Somot, S. (2013). Interannual variability of deep convection in the Northwestern Mediterranean simulated with a coupled AORCM. *Climate Dynamics*, *41*(3–4), 937–960. https://doi.org/10.1007/s00382-012-1527-5

Ludwig, W., Dumont, E., Meybeck, M., & Heussner, S. (2009). River discharges of water and nutrients to the Mediterranean and Black Sea: Major drivers for ecosystem changes during past and future decades? *Progress in Oceanography*, *80*(3), 199–217.

Luo, H., Bracco, A., & Zhang, F. (2014). The seasonality of convective events in the Labrador Sea. *Journal of Climate*, *27*(17), 6456–6471.

Madec, G. (2008). *NEMO ocean engine, note du Pôle de modélisation*. Paris, France: Institut Pierre-Simon Laplace.

Madec, G., Chartier, M., Delecluse, P., & Crépon, M. (1991). A three-dimensional numerical study of deep-water formation in the Northwestern Mediterranean Sea. *Journal of Physical Oceanography*, *21*(9), 1349–1371.

Marchesiello, P., Capet, X., Menkes, C., & Kennan, S. C. (2011). Submesoscale dynamics in tropical instability waves. *Ocean Modelling*, *39*(1), 31–46.

Marshall, J., & Schott, F. (1999). Open-ocean convection: Observations, theory, and models. *Reviews of Geophysics*, *37*, 1–64.

MEDOC-Group (1970). Observations of formation of deep-water in the Mediterranean Sea. *Nature*, *227*, 1037–1040.

Mertens, C., & Schott, F. (1998). Interannual variability of deep-water formation in the Northwestern Mediterranean. *Journal of Physical Oceanography*, *28*, 1410–1424.

Millot, C. (1991). Mesoscale and seasonal variabilities of the circulation in the Western Mediterranean. *Dynamics of Atmospheres and Oceans*, *15*, 179–214.

Millot, C. (1999). Circulation in the Western Mediterranean Sea. *Journal of Marine Systems*, *20*, 423–442.

Paquin, J.-P., Lu, Y., Higginson, S., Dupont, F., & Garric, G. (2016). Modelled variations of deep convection in the Irminger Sea during 2003–10. *Journal of Physical Oceanography*, *46*(1), 179–196.

Penduff, T., Juza, M., Barnier, B., Zika, J., Dewar, W. K., Treguier, A.-M., Molines, J.-M., & Audiffren, N. (2011). Sea level expression of intrinsic and forced ocean variabilities at interannual time scales. *Journal of Climate*, *24*(21), 5652–5670.

Radu, R., Déqué, M., & Somot, S. (2008). Spectral nudging in a spectral regional climate model. *Tellus, Series A*, *60*, 898–910. https://doi.org/10.1111/j.1600-0870.2008.00341.x

Rugenstein, M., Winton, M., Stouffer, R. J., Griffies, S. M., & Hallberg, R. (2013). Northern high-latitude heat budget decomposition and transient warming. *Journal of Climate*, *26*, 609–621.

Saenko, O. A., Dupont, F., Yang, D., Myers, P. G., Yashayaev, I., & Smith, G. C. (2014). Role of resolved and parameterized eddies in the Labrador Sea balance of heat and buoyancy. *Journal of Physical Oceanography*, *44*(12), 3008–3032.

Sannino, G., Herrmann, M., Carillo, A., Rupolo, V., Ruggiero, V., Artale, V., & Heimbach, P. (2009). An eddy-permitting model of the Mediterranean Sea with a two-way grid refinement at the Strait of Gibraltar. *Ocean Modelling*, *30*(1), 56–72. https://doi.org/10.1016/j.ocemod.2009.06.002

Santinelli, C., Hansell, D. A., & Ribera d'Alcalà, M. (2013). Influence of stratification on marine dissolved organic carbon (DOC) dynamics: The Mediterranean Sea case. *Progress in Oceanography*, *119*, 68–77.

Schott, F., Visbeck, M., Send, U., Fisher, J., Stramma, L., & Desaubies, Y. (1996). Observations of deep convection in the Gulf of Lions, northern Mediterranean, during the winter of 1991/1992. *Journal of Physical Oceanography*, *26*, 505–524.

Sérazin, G., Meyssignac, B., Penduff, T., Terray, L., Barnier, B., & Molines, J.-M. (2016). Quantifying uncertainties on regional sea level change induced by multidecadal intrinsic oceanic variability. *Geophysical Research Letters*, *43*, 8151–8159. https://org.doi/10.1002/2016GL069273

Sérazin, G., Penduff, T., Grégorio, S., Barnier, B., Molines, J.-M., & Terray, L. (2015). Intrinsic variability of sea level from global ocean simulations: Spatiotemporal scales. *Journal of Climate*, *28*(10), 4279–4292.

Somot, S., Houpert, L., Sevault, F., Testor, P., Bosse, I., Taupier-Letage, A., . . . Herrmann, M. (2016). Characterizing, modelling and understanding the climate variability of the deep water formation in the North-Western Mediterranean Sea. *Climate Dynamics*, 1–32. https://doi.org/10.1007/s00382-016-3295-0

Somot, S., Sevault, F., & Déqué, M. (2006). Transient climate change scenario simulation of the Mediterranean Sea for the 21st century using a high resolution ocean circulation model. *Climate Dynamics*, *27*, 851–879. https://doi.org/10.1007/s00382-006-0167-z

Stammer, D., & Wunsch, C. (1999). Temporal changes in eddy energy of the oceans. *Deep Sea Research Part II: Topical Studies in Oceanography*, *46*(1), 77–108.

Stanev, E. V., & Peneva, E. L. (2001). Regional sea level response to global climatic change: Black sea examples. *Global and Planetary Change*, *32*(1), 33–47.

Taillandier, V. (2014). *CTD dataset acquired during the field survey DEWEX* (technical report). Retrieved from ftp://oceane.obs-vlfr.fr/pub/prieur/GC/Dewex2013leg1_leg2_ASCII/DEWEX2013-CTDreport.pdf

Talandier, C., Deshayes, J., Treguier, A.-M., Capet, X., Benshila, R., Debreu, L., . . . Madec, G. (2014). Improvements of simulated Western North Atlantic current system and impacts on the AMOC. *Ocean Modelling*, *76*, 1–19. https://doi.org/10.1016/j.ocemod.2013.12.007

Tamburini, C., Canals, M., Durrieu de Madron, X., Houpert, L., Lefèvre, D., Martini, S., . . . Zúñiga, J. (2013). Deep-sea bioluminescence blooms after dense water formation at the ocean surface. *PLoS ONE*, *8*(7), e67523. Retrieved from http://campagnes.flotteoceanographique.fr/campagnes/13020010/

Testor, P. (2013). *DEWEX-MERMEX 2013 LEG1 cruise, le Suroit R/V* (technical report). Retrieved from http://campagnes.flotteoceanographique.fr/campagnes/13020010/

Testor, P., Coppola, L., & Mortier, L. (2012). *2012 MOOSE-GE cruise, le Suroit R/V* (technical report). Retrieved from http://campagnes.flotteoceanographique.fr/campagnes/12020030/index.htm

Testor, P., Coppola, L., & Mortier, L. (2013). *2013 MOOSE-GE cruise, Tethys ii R/V* (technical report). Retrieved from http://campagnes.flotteoceanographique.fr/campagnes/13450110/index.htm

Testor, P., Durrieu de Madron, X., Mortier, L., D'ortenzio, F., Legoff, H., Dausse, D., . . . Houpert, L. (2016). *LION observatory data* (technical report). Retrieved from http://www.seanoe.org/data/00333/44411/

Testor, P., & Gascard, J.-C. (2003). Large-scale spreading of deep waters in the Western Mediterranean Sea by submesoscale coherent eddies. *Journal of Physical Oceanography*, *33*, 75–87.

Testor, P., & Gascard, J.-C. (2006). Post-convection spreading phase in the Northwestern Mediterranean Sea. *Deep Sea Research Part I: Oceanographic Research Papers*, *53*, 869–893.

Thompson, A. F., & Naveira Garabato, A. C. (2014). Equilibration of the Antarctic Circumpolar Current by standing meanders. *Journal of Physical Oceanography*, *44*(7), 1811–1828.

Tziperman, E. (1986). On the role of interior mixing and air-sea fluxes in determining the stratification and circulation of the oceans. *Journal of Physical Oceanography*, *16*, 680–693.

Tziperman, E., & Speer, K. (1994). A study of water mass transformation in the Mediterranean Sea: Analysis of climatological data and a simple three-box model. *Dynamics of Atmospheres and Oceans*, *21*, 53–82.

Visbeck, M. J., Marshall, J., & Jones, H. (1996). Dynamics of isolated convective regions in the ocean. *Journal of Physical Oceanography*, *26*, 1721–1734.

von Storch, J.-S., Eden, C., Fast, I., Haak, H., Hernandez-Deckers, D., Maier-Reimer, E., . . . Stammer, D. (2012). An estimate of the Lorenz energy cycle for the world ocean based on the STORM/NCEP simulation. *Journal of Physical Oceanography*, *42*(12), 2185–2205. https://doi.org/10.1175/JPO-D-12-079.1

Vörösmarty, C., Fekete, B., & Tucker, B. (1996). *Global river discharge database, RivDis*. Paris, France: UNESCO, International Hydrological Program, Global Hydrological Archive and Analysis Systems.

Waldman, R., Somot, S., Herrmann, M., Bosse, A., Caniaux, G., Estournel, C., . . . Testor, P. (2017). Modeling the intense 2012–2013 dense water formation event in the northwestern Mediterranean Sea: Evaluation with an ensemble simulation approach. *Journal of Geophysical Research: Oceans*, *122*, 1297–1324. https://doi.org/10.1002/2016JC012437

Waldman, R., Somot, S., Herrmann, M., Testor, P., Estournel, C., Sevault, F., . . . & Dausse, D. (2016). Estimating dense water volume and its evolution for the year 2012–2013 in the Northwestern Mediterranean Sea: An observing system simulation experiment approach. *Journal of Geophysical Research: Oceans*, *121*, 6696–6716. https://doi.org/10.1002/2016JC011694

Walin, G. (1977). A theoretical framework for the description of estuaries. *Tellus*, *29*(2), 128–136.

Walin, G. (1982). On the relation between sea-surface heat flow and the thermal circulation in the ocean. *Tellus*, *34*, 187–195.

Winton, M., Griffies, S. M., Samuels, B. L., Sarmiento, J. L., & Frolicher, T. L. (2013). Connecting changing ocean circulation with changing climate. *Journal of Climate*, *26*, 2268–2278.

Wunsch, C. (2002). What is the thermohaline circulation? *Science*, *298*(5596), 1179–1181.